

Use Authorization

In presenting this thesis in partial fulfillment of the requirements for an advanced degree at Idaho State University, I agree that the Library shall make it freely available for inspection. I further state that permission to download and/or print my thesis for scholarly purposes may be granted by the Dean of the Graduate School, Dean of my academic division, or by the University Librarian. It is understood that any copying or publication of this thesis for financial gain shall not be allowed without my written permission.

Signature _____

Date _____

2-D Shape Classification Using Moments Invariants and Fractal Geometry in the Presence of Noise

By

Adel Alsaraj

B. SC. Electrical Engineering

A Thesis Submitted to the

Idaho State University

in Partial Fulfillment of the Requirements for the degree of

MASTER OF SCIENCE

in

Measurement and Control Engineering

Under the Supervision of

Dr. Dawid Zydek

To the Graduate Faculty:

The members of the committee appointed to examine the thesis of Adel Alsaraj find it satisfactory and recommend that it be accepted.

Dr. Dawid Zydek, Major Advisor, Electrical Engineering

Signature _____ Date _____

Dr. Steve Chiu, Co-Advisor, Electrical Engineering

Signature _____ Date _____

Dr. Jason Harris, GFR, Nuclear Engineering & Health Physics

Signature _____ Date _____

TABLE OF CONTENTS

LIST OF FIGURES	vi
LIST OF TABLES	viii
ABSTRACT	ix
Introduction	1
1.1. Overview.....	1
1.2. Problems of Interest	1
1.3. Fractal Geometry Application Directions.....	2
1.4. Thesis Outline	4
Background	5
2.1. Shape Analysis.....	5
2.2. Fractal Geometry	6
2.3. Fractional Brownian motion (<i>fBm</i>).....	10
2.4. Neural Network (NN) Classifiers	13
2.5. Moment Theory	16
Fractal Feature Extraction	19
3.1. Introduction.....	19
3.2. Fractal Dimension Concept	20
3.3. Fractal dimension computation.....	25
3.4. Fractal Signature	29
Fractal-Based Approach for Target Recognition	32
4.1. Three-View Fractal Target Recognition.....	32
4.2. Noise-tolerant fractal signature.....	34
4.3. Moments invariant	36

4.4. Classification results and discussion.....	38
Conclusions.....	43
5.1. Conclusions.....	43
5.2. Future Research Plan	43
References.....	44

LIST OF FIGURES

Figure 1-1: Block diagram of typical ATR system.....	1
Figure 2-1: Some fractal structures.....	6
Figure 2-2: Von Koch curve at different iterations.....	7
Figure 2-3: Self similarity of reduced objects and the original object.....	9
Figure 2-4: Samples of fractional Brownian motion traces vs. t for different values of H and D from up to bottom.....	12
Figure 2-5: Fractal Brownian motion (fBm) signals with different H values.	13
Figure 2-6: A simple 2x3x1 NN.	15
Figure 3-1: A special photocopy machine with reduction factor of 1/3.	21
Figure 3-2: Self-similarity of line, square, and cube.	22
Figure 3-3: Results of Richardson's experiment	24
Figure 3-4: An irregular structure with some scaling properties.....	25
Figure 3-5: The front view of Mirage 2000.....	26
Figure 3-6: The Radii profile of the front view of Mirage 2000.	27
Figure 3-7: Law verification and calculation of fractal dimension (D).....	27
Figure 3-8: Fractal dimension at different scale percentage.....	28
Figure 3-9: Fractal dimension at different rotational angles.....	29
Figure 3-10: Radii profile for a boundary of a shape.	30
Figure 3-11: Fractal signatures for simple shapes.	31

Figure 4-1: The views of the five classes of aircraft under study.....	33
Figure 4-2: T^H verification for Mirage 2000 side view, RMSE=0.02.....	33
Figure 4-3: Histogram for mirage 2000 side view boundary.....	34
Figure 4-4: Robustness of signature and Fourier descriptors.	35
Figure 4-5: Fractal signature with different noise values.	35
Figure 4-6: Abstracted fractal signature with different noise values.....	36
Figure 4-7: Moments invariant parameters for different scaling values.....	38
Figure 4-8: Moments invariant parameters for different rotational angles.....	38
Figure 4-9: B57 front view with normal noise of zero mean and standard deviation values: 1, 2, 3, 4, 5 from left to right respectively.....	39
Figure 4-10: Representative example of clean and noisy test images.	39
Figure 4-11: Classification results of abstracted fractal signature and moments invariant under different degrees of noise.....	41
Figure 4-12: Aircraft views samples at different orientations.	42

LIST OF TABLES

Table 4-1: Fractal abstracted signature of some aircraft views.	35
Table 4-2: Confusion matrix of the results of neural net classifier with abstracted fractal signature input.	40
Table 4-3: Recognition results for tilt and yew operations.	42

ABSTRACT

This thesis addresses the problem of target image processing. The thesis presents a noise-tolerant procedure for classifying targets based on fractal analysis of three-view (top, side, and front) projections. The boundary of aircraft has been shown to have fractional Brownian motion behavior. A set of fractal features has been extracted. These features are fractal Dimension, and noise-tolerant fractal signature feature vector. Fractal dimension and fractal signature are considered invariant under rotation, translation, and scaling. Fractal dimension provides a good feature for discriminating classes that have different roughness (e.g. mountains and aircraft), but in the case of close roughness levels (e.g. aircraft types), fractal signature is used. The fractal signature has also been abstracted in terms of five features to overcome the problem of sensitivity to noise. The classification stage has been achieved using neural networks. The training of the neural network is performed using five types of aircraft and three viewing angles (top, side, and front) per each one. Three-view targets at arbitrary viewing angles and range have been presented to a three-layer back propagation neural net classifier. A comparative study between fractal based features and moment invariants is developed under clean and noisy conditions. Classification results have indicated superior performance of fractal features over moment invariant features. Under normal noise effect of zero mean and standard deviation equal two, the average percentage of correct recognition has been about 90% for the proposed system compared to 40% for the traditional moment invariants method.

CHAPTER 1

INTRODUCTION

1.1. Overview

One of the key components of present and future defense weapon systems to be used on autonomous vehicle missions is the Automatic Target Recognition (ATR) system. Multi-sensor ATR system effectively removes man from the process of target acquisition and recognition. This is desirable since the system with a man in the loop is generally slow, unreliable, and may limit the performance of the overall system or mission in real situations [1] [2].

The algorithmic components of an ATR system can be decomposed into preprocessing, detection, segmentation, feature computation, selection and classification, prioritization, tracking, and aim point selection as shown in Figure 0-1 [1]. The main focus of this thesis is the target feature computation and classification based on target processing as shown in Figure 0-1.

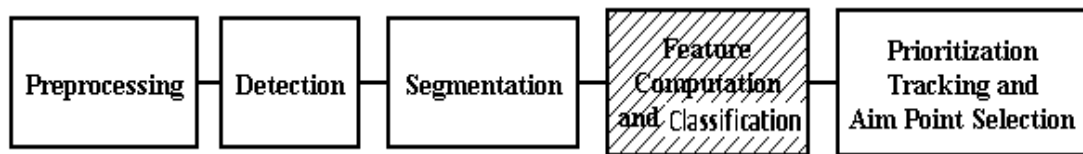


Figure 0-1: Block diagram of typical ATR system

1.2. Problems of Interest

This thesis is essentially concerned with three-view target image processing. Targets have been recognized based on the fractal analysis of their three-view (Top, Side, and Front). Target classification has been performed through the study and analysis of the following main items:

- I. The fractional Brownian motion behavior of three-views (Top, Side, Front) of five types of aircraft (Mirage 2000, B57, Beech Craft, F15, TU-160), with total of fifteen images.

- II. Fractal feature extraction with focus on: fractal Dimension (D) and fractal signature.
- III. The computation of an improved Noise-Tolerant Fractal Signature (NTFS)
- IV. The application of neural net for classification of aircraft views based on the abstracted noise-tolerant fractal signature feature vector.
- V. A comparative study among the following: The abstracted noise-tolerant fractal signature, fractal signature & Fourier Descriptors (FD), and moment invariant in the classification robustness, especially under different levels of noise.

1.3. Fractal Geometry Application Directions

Many problems in the analysis of natural surface shapes and the construction of terrain maps to model them remain unsolved. One reason is that the familiar Euclidean geometry of regular shapes, such as surfaces of revolution, does not capture well irregular and less structured shapes.

Hongteng in [2] proposed a single image super resolution and enhancement algorithm using local fractal analysis. According to the scale invariance (a special case of bi-Lipschitz invariance) feature of fractal dimension, the gradient of a high-resolution image from that of a low-resolution one, was estimated. A regularization term based on the scale invariance of fractal dimension and length was shown to be effective in recovering details of the high-resolution image. Analysis was provided on the relation and difference among the proposed approach and some other state of the art interpolation methods. Experimental results showed that the proposed method has superior super-resolution and enhancement results as compared to other competitors.

In [3], Wenhui searched for a method of developing fractal analysis module in ArcGIS software, calculating fractal-dimension by box-counting and processing some elementary research on fractal characteristics of rivers with this module.

Another application of fractal geometry is image compression. Image compression using fractal geometry has received great attention in recent years. Fractal compression is quite controversial, with some people claiming it does not work well, and others claiming it works wonderfully. The basic idea behind fractal image compression is to express the image as an Iterated Function System (IFS). The image can then be displayed quickly and zooming will generate infinite levels of (synthetic) fractal detail. The problem is how to

efficiently generate the IFS from the image. Barnsley, who invented fractal image compression, has a patent on fractal compression techniques [4] [5] [6] [7].

Mandelbrot proposed fractals as a family of mathematical functions to describe natural phenomena such as coastlines, mountains, branch patterns of trees and rivers, clouds, and earthquakes [8]. Since Mandelbrot introduced them, fractal sets and functions have been found to describe many other environmental properties, and have received a great deal of attention from scientists, artists, and others.

Researchers in computer graphics and image understanding have applied fractal theory to a variety of problems. In computer graphics, fractals have been used to synthesis models of complex natural objects such as trees, mountain ranges, and clouds. The rendered images and models exhibit a high level of realism compared to previous efforts. In image understanding, fractals have been employed to analyse projections of natural scenes. For modelling shapes of natural objects, Pentland in [9] presented a method to estimate fractal dimension from the "second-order statistics" of image intensities. He showed that measurements of fractal dimension might be used to measure perspective gradient, thus providing an independent check on estimates of surface orientation derived from analysis of foreshortening.

Keller in [10] estimated the fractal dimension using a least-square linear fit, and used it to distinguish silhouettes of trees from silhouettes of mountains.

For segmenting textured surfaces, Pentland in [9] computed a self-similarity parameter and used it to segment real images of scenes of urban areas, mountains, and deserts. He reported classification accuracy of 84 and 88% on Brodatz texture patterns.

Yasumoto reported that fractal dimension alone does not provide sufficient discriminatory power to classify natural textures [11]. His results are confirmed by Keller [12], who used estimates of fractal dimension together with features based on the concept of lacunarity as global signatures of texture and as local measurements of texture for segmentation purposes. They presented segmentation results for eight Brodatz texture patterns, an outdoor scene, and a variety of artificial patterns.

For interpolating natural surfaces, Yokoya adopted a recursive midpoint displacement scheme using four neighbours to interpolate natural surfaces [13]. They computed two features, a self-similarity parameter, and the standard deviation of the distribution function; and use them for stochastic interpolation in order to preserve the statistical characteristics

of the true surface. The work on modelling natural shapes, segmenting textured surfaces, and interpolating natural surfaces represents significant advances.

1.4. Thesis Outline

Fractal geometry has been played an important role in a variety of applications. In this thesis, our approach is using fractal features in the classification of aircraft's three-views. All classifiers have been implemented using neural net classifiers.

In chapter 2, "Fractal Geometry: An Overview", a theoretical background and concepts of all topics used in this thesis are presented.

In chapter 3, "Fractal Feature Extraction", the role of feature extraction stage in automatic target recognition is explained.

In chapter 4, "Fractal-Based Approach for Target Recognition", addresses the problem of three-view ATR.

In chapter 5, "Conclusions", a summary and Conclusions of research effort in the thesis are provided along with potential future research directions.

CHAPTER 2

BACKGROUND

This chapter begins with an introduction to shape analysis in Section 2.1. A definition of fractals, and a brief history of the fractal geometry science, and the role of Mandelbrot, who is considered the father of the fractal geometry, is presented in Section 2.2. A method to generate the Koch curve, as an example to a fractal pattern, is presented in the Section. The role of fractal geometry in image recognition is discussed. Image recognition techniques based on fractal features like D, AHC, and fractal signature are presented. Fractal geometry is considered a new geometrical science that deals with the natural phenomena, which cannot be represented or analyzed using classical geometry. The concepts of exact self-similarity and statistical self-similarity, the backbone of fractal geometry are discussed. The Brownian motion, which has been observed by Robert Brown in 1827, is stated and analyzed, and then the fractional Brownian motion and its mathematics are introduced in Section 2.3. The classification tests in this thesis are performed using neural nets. The structure of the back propagation neural net classifier and its learning algorithm are generally discussed in Section 2.4. The moment theory, the definition of moment in 2-D, and the central moment are discussed in Section 2.5. The SDP plots are discussed, and its applications in signal processing and visual classification tests are identified in Section 2.6.

2.1. Shape Analysis

The interaction between light and surrounding objects provides an important means for humans to understand the world. This is clear if we consider that 50% of our brain is involved in visual information processing. Giving the machine the ability to automate dangerous or repetitive human activities requires effective machine vision systems.

The birth of computer vision started very early in computer history. There is a great deal of machine vision application in biology, security, robotics, industry, and physics. For humans “seeing” appears to be a trivial task, but designing robust machine vision systems has been difficult. This is because machine vision systems require real-time processing of a huge data set (including shape, color, spatial orientation, motion, texture, etc.).

More difficulties with the analysis of visual information arise from distortions, occlusion, and noise, besides the requirement to map image from 3-D space onto 2-D space which lead to information loss.

Shapes analysis can be thought as being the alphabet of the visual language. 2D-object object has enough information allowing the recognition of the original object.

Dealing with 3D representation of objects is computationally expensive, so the importance of 2D image analysis arises to solve this problem.

2.2. Fractal Geometry

A fractal shape is a rough geometric shape that can be divided into smaller parts, each part is an exact reduced copy of the original shape or at least approximately similar to the original shape.

Fractals are generally self-similar and independent of scale. There are many mathematical structures that are fractals; e.g. Sierpinski triangle, Koch snowflake, Peano curve, Mandelbrot set, and Lorenz attractor, as shown in Figure 2-1. Fractals also describe many real-world objects, such as clouds, mountains, coastlines, roots, branches of trees, blood vessels, and lungs of animals that do not correspond to simple geometric shapes. Benoit B. Mandelbrot gives a mathematical definition of a fractal as a set of which the Hausdorff Besicovich dimension strictly exceeds the topological dimension. The corresponding Latin verb “frangere” means "to break:" to create irregular fragment [8]

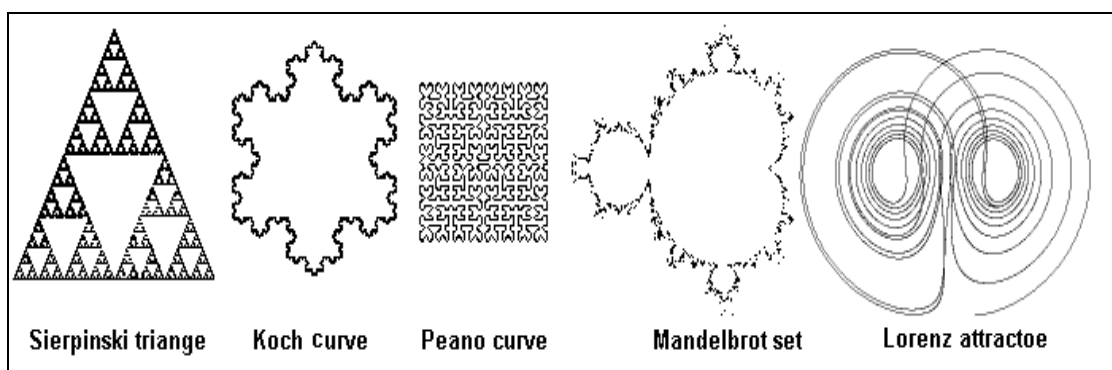


Figure 2-1: Some fractal structures

Mandelbrot is often characterized as the father of fractal geometry. Mandelbrot demonstrated that these early mathematical fractals have many features in common with

shapes found in nature. The best way to describe his contribution is to say that, indeed, some characters, such as the Cantor set, were already there but he went on to develop the language into which the characters could be embedded [14]. An algorithm of generating a fractal shape, Koch curve, is shown in Section 2.2.1.

2.2.1. Generating Koch curve

To produce the geometric construction of Koch curve, begin with a straight line, which is called the initiator. Partition it into three equal parts. Then replace the middle third by equilateral triangle and take away its base. This completes the basic construction step. A reduction of this figure, made of four parts, will be reused in the following stages. It is called the generator. Thus, we now repeat, taking each of the resulting line segments, partitioning them into their equal parts, and so on. Figure 2-2 illustrates the first five steps. Self-similarity is built into the construction process, i.e. each part of the 4 parts in the K^{th} step is again a scaled down version by a factor of 3 of the entire curve in the previous $(K-1)^{\text{st}}$ steps [14].

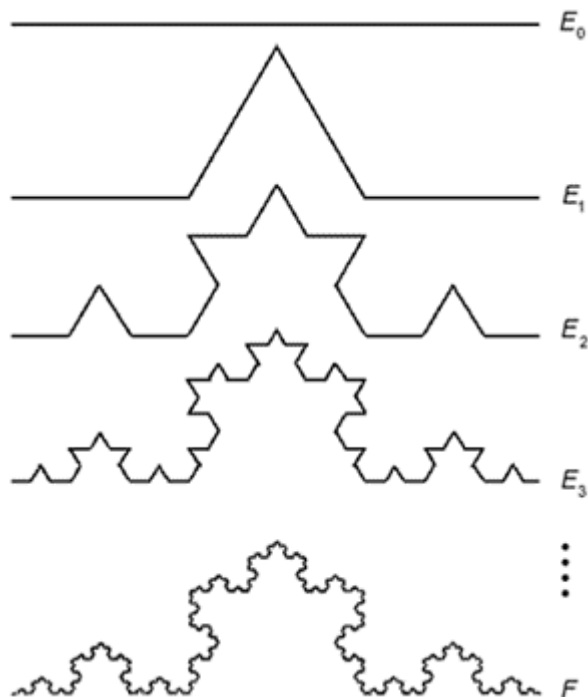


Figure 2-2: Von Koch curve at different iterations.

2.2.2. Object segmentation based on fractal features

For segmentation and recognition of objects in natural scenes, there is always a need for features that are invariant to scale, rotation, and translation of the object. Fractal geometry provides fractal features that can be computed from image. Fractal dimension is the primary fractal feature that can be computed from images. Fractal dimension is scale, rotation, and translation invariant, so it is convenient as a feature for target recognition applications. There are several methods to estimate fractal dimension of a fractal surface. Some of these methods and its implementations will be discussed in chapter 3. Some rely on a specific fractal model, such as fractional Brownian motion, whereas others are applicable to a wider class of fractals, such as box counting method [15]

Another fractal feature related to fractal dimension but sensitive to scale is the Average Holder Constant (AHC). AHC can give an estimate to scale as well as range of an object. A technique for implementing AHC will be discussed in chapter 3.

A three fractal features that is scale, rotation, and translation invariant is the fractal signature. While fractal dimension is suitable for classifying objects with different roughness measure (H), it is not capable for classifying objects with the same roughness measure. Fractal signature, however, can classify objects which have the same roughness measure with the same fractal dimension. More depicted analysis and test results for the three fractal features will be presented through this thesis. The concept of fractal dimension is always related to the self-similarity property of a fractal shape. There are two types of fractal self-similarity, exact self-similarity in Section 2.2.3, and statistical self-similarity in Section 2.2.4.

2.2.3. Exact self-similarity

Self-similarity extends one of the most fruitful notions of elementary geometry: similarity. Two objects are similar if they have the same shape, regardless of their size. Corresponding angles, however, must be equal, and corresponding line segments must all have the same factor of proportionality. For example, when a photo is enlarged, it is enlarged by the same factor in both horizontal and vertical directions. Even an oblique, i.e. non-horizontal, non-vertical, line segment between points in the original will be enlarged by the same factor as shown in in Figure 2-3. We call this enlargement factor-scaling factor. The transformation between the objects is called similarity transformation [14].

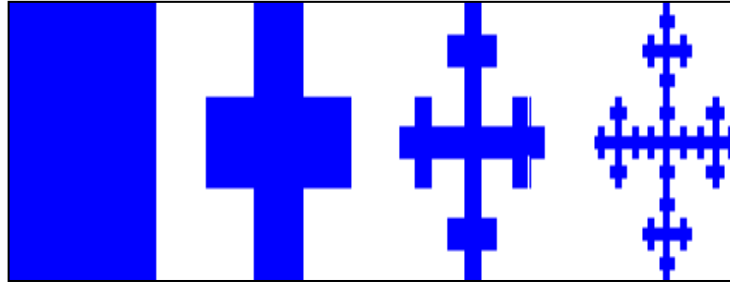


Figure 2-3: Self similarity of reduced objects and the original object.

2.2.4. Statistical self-similarity

The exact self-similarity of Von Koch curve may be considered a crude model for a coastline, but it differs from the coastline in one significant aspect, upon magnification segments of the coastline look like, but never exactly like, segments at different scales. The concept of fractal dimension, however, can be also applied to such statistical self-similarity object. In a measurement of the length of a coastline, the more carefully one follows the smaller wiggles, the longer it becomes. Walking along a beach is longer than driving along corresponding coast highway. Moreover, each small section of a coastline looks like (but not exactly like) a larger portion. When using a ruler of size r to measure a coastline's length, the total length equals the ruler size r times the number of steps of size r , $N(r)$, taken in tracing the coast Length.

As with the snowflake, $N(r)$ varies on the average as $\frac{1}{r^D}$ and

$$\text{Length} \propto r \times \frac{1}{r^D} \quad (2.1)$$

Where D is the fractal dimension. With $D > 1$, as the size of the ruler, used to measure a coast, decreases, the length increases. The variation of apparent coast length with ruler size has been studied by Richardson as summarized in [8]. Real coastlines can, in fact, be characterized by fractal dimension D of about 1.5 to 1.25, close to that of Von Koch curve.

The property that objects can look statistically similar while at the same time different in detail at different length scales, is the central feature of fractals in nature [16].

2.3. Fractional Brownian motion (*fBm*)

2.3.1. Brownian motion

Brownian motion is named after Botanist Robert Brown, who first observed the phenomena in 1827. Brownian motion is the motion of small particles caused by continual bombardment by other neighboring particles. We can see Brownian motion by observing a drop of water through a microscope. Small particles of dust and dirt in the water droplet always appear to be in constant random motion. The dust particles are constantly bombarded by millions of surrounding water molecules. The water molecules are always moving because of the thermal agitation caused by the water being room temperature. Due to the huge numbers of molecules in the water drop that are moving in virtually all directions, the average position of the dust particles remains the same. The dust particles are simply agitated back and forth as they are struck repeatedly.

To analyze the structure of Brownian motion, let's consider what happens if we restrict the motion to one dimension. In other words, the particle can only move along the x -axis and can only be struck from the left or right. As a further simplification, assume that each impact moves the particle a fixed distance, known as l , to the left or right (each water molecule transfers the same momentum to the particle) and that only one impact occurs at a time. The particle starts at position 0 on the x -axis. Because the particle can be struck from the left or right with equal probability, we would expect the particle to remain at 0 generally. We will probably find the average deviation of the particle position from the origin of greater interest. The most common way to measure the deviation is to measure the square of the distance of the particle position from its initial position. In probabilistic terms, the square of this distance is the variance of the particle position. You can easily show that the variance of particle position is simply $n * l * l$, where n is the number of times the particle is struck while it is being observed and l is the distance of the particle from the origin. Assuming that the particle is bombarded at a constant rate (meaning n is proportional to the length of time you observe the particle), and then the variance of the particle from its initial position is proportional to $t * l * l$ where t is the observation time. So, the longer we observe the particle, the more likely the particle moves away from its initial position. Because the variance is a measure of the square of the particle-position change, the absolute value of the change in particle position is the square root of the

variance. In this case, the standard deviation of the particle position is equal to $\sqrt{t} * l$. More formally, we can represent the position of the particle as a random variable X . A water molecule striking the particle can be considered as a sample of a random variable L , where L can take on only one of two possible values, either $+l$ (struck from the left) or $-l$ (struck from the right). So, we can write X as the sum of L_i , where the L_i are summed over all instances of the particle being struck. This results in equation (2.2).

$$X(n) = \sum_{i=1}^n L(i) \quad (2.2)$$

Where $i=1, 2, 3, \dots, n$.

Each $L(i)$ is independent and identically distributed. It will take on the value $+l$ or $-l$ with equal probability. From equation (2.2), it can be seen that the mean value for $X(n)$ is 0 because the mean value of each L_i is 0. Furthermore, the variance of each L_i is (l^2) . So, the variance of X is $n * l^2$, as explained earlier. Finally, for large n , the central-limit theorem of probability states that the distribution of X will be Gaussian because X is the sum of independent, identically distributed random variables. The assumption of large n is quite valid for any reasonable length of time.

Perhaps the most interesting feature of Brownian motion is the property that the variance in particle position increases linearly over the time of observation. Furthermore, this property holds, no matter when you start the observation. It is therefore independent of any particular starting time for the measurement. The distribution of particle position is always Gaussian, with a variance dependent solely on the length of your observation. Given an initial measurement of the variable X at a particular starting time, the position at any subsequent time is a random variable whose mean is the initial position, and whose variance is proportional to the difference in time from the initial position. Mathematically, this property reduces to the condition specified by equation (2.2), where $Var(X)$ is the variance of the random variable X .

$$\begin{aligned} Var(X(t_2) - X(t_1)) &= K * |t_2 - t_1| * l^2 \\ &= |t_2 - t_1| * Q * Q \end{aligned} \quad (2.2)$$

Where k is proportionality constant.

In (2.2), the number of particle strikes has been replaced by the observation time t because n is assumed to be proportional to t . The proportionality constant k simply provides the proper scaling between time measurements and particle strikes. In general, the factor k is simply absorbed into the l^2 factor and denoted by a single constant $Q * Q$. It can

be easily verify (2.2) by substituting in the definition for $X(t_2)$ and $X(t_1)$, making the appropriate substitutions of time t for particle strikes [17].

2.3.2. Mathematical concept of fractional Brownian motion

One of the most useful models for the random fractal found in nature (such as mountain terrain and clouds) has been the fractional Brownian motion of Mandelbrot and Van Ness [8]. It is an extension of the concept of Brownian motion that has played an important role in both physics and mathematics. Almost all natural computer graphics fractal simulations are based on an extension of fBm to higher dimension [16]. As can be seen from the sample traces of fBm in Figure 2-4, a fractional Brownian motion, $V_H(t)$, is a single valued function of one variable, t (usually time). In appearance, it is reminiscent of a mountain horizon or fluctuations of an economic variable. The scaling behavior of the different traces in Figure 2-4 is characterized by a parameter H in the range $0 < H < 1$, when H is close to 0 the traces are roughest while those with H close to 1 are relatively smooth. H relates the typical change in V , $\Delta V = V(t_2 - t_1)$, to the time difference $\Delta t = t_2 - t_1$ by the simple scaling law:

$$\Delta V \propto \Delta t^H \quad (2.3)$$

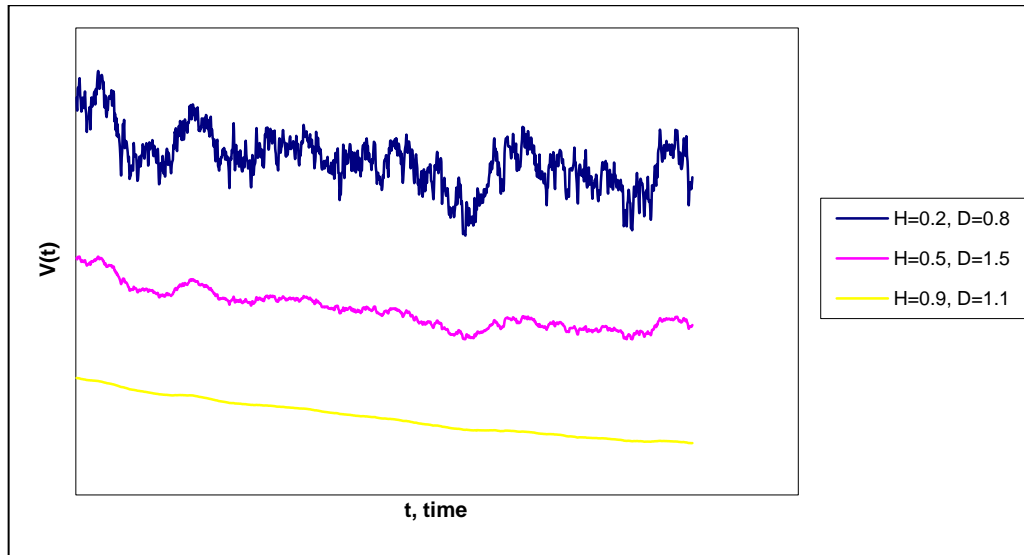


Figure 2-4: Samples of fractional Brownian motion traces vs. t for different values of H and D from up to bottom.

In the usual Brownian motion or random walk, the sum of independent increments or steps leads to a variation that scales as the square of the number of steps. Thus, $H=1/2$ corresponds to a trace of Brownian motion.

A generation of one dimensional fractal Brownian motion signals with different roughness measure (H) using the algorithm discussed before is shown in Figure 2-5.

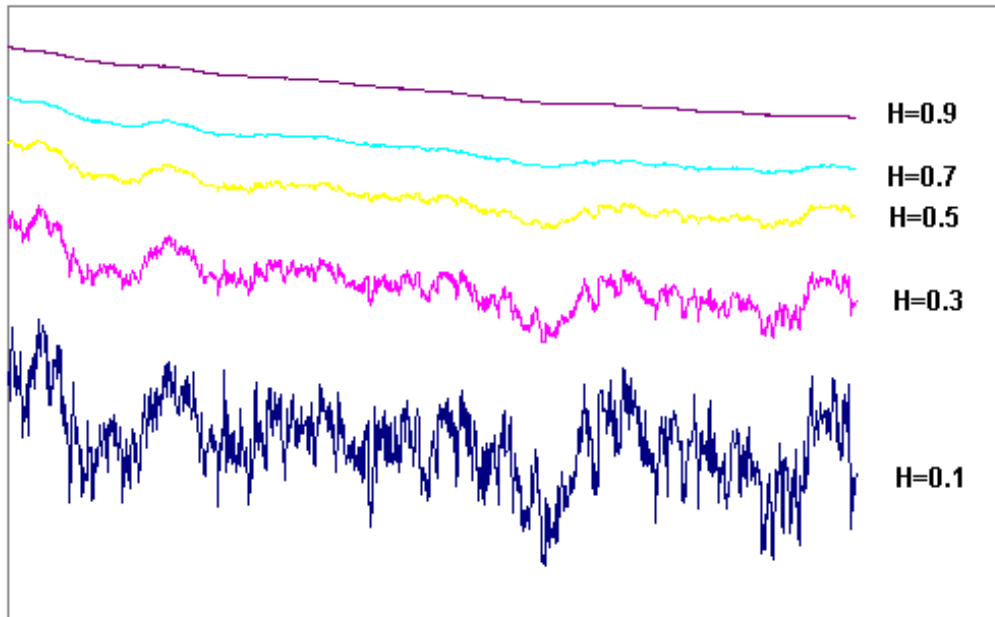


Figure 2-5: Fractal Brownian motion (*fBm*) signals with different H values.

2.4. Neural Network (NN) Classifiers

Artificial Neural Net is a network of many simple processors ("units"), each possibly having a small amount of local memory. Communication channels ("connections"), which usually carry numeric (as opposed to symbolic) data, encoded by any of various means connect the units. The units operate only on their local data and on the inputs they receive via the connections. The restriction to local operations is often relaxed during training [18] [19] [20].

Some NNs are models of biological neural networks and some are not. But historically, much of the inspiration for the field of NNs came from the desire to produce artificial systems capable of sophisticated, perhaps "intelligent", computations similar to those that the human brain routinely performs, and thereby possibly to enhance our understanding of the human brain.

Most NNs have some sort of "training" rule, whereby the weights of connections are adjusted on the basis of data. In other words, NNs "learn" from examples (as children learn to recognize dogs from examples of dogs) and exhibit some capability for generalization beyond the training data.

NNs normally have great potential for parallelism, since the computations of the components are largely independent of each other.

There are many kinds of NNs. Nobody knows exactly how many. New ones (or at least variations of existing ones) are invented every week. The main categorization of these methods is the distinction between supervised and unsupervised learning. In supervised learning, there is a "teacher" who in the learning phase "tells" the net how well it performs ("reinforcement learning") or what the correct behavior would have been. In unsupervised learning the net is autonomous: it just looks at the data, it is presented with, finds out about some of the properties of the data set and learns to reflect these properties in its output. What exactly these properties are, that the network can learn to recognize, depends on the particular network model and learning method. Usually, the net learns some compressed representation of the data. Many of these learning methods are closely connected with a certain network topology. Some unsupervised learning NNs existing now are Additive Grasberg, Shunting Grasberg, Binary Adaptive Resonance, Discrete Hopfield, Continuous Hopfield, Discrete Bi-directional Associative Memory, Temporal Associative Memory, Kohonen Self-organizing, Competitive Learning, Learning Matrix, Linear Associative Memory, Optimal Linear Associative Memory, Sparse Distributed Associative Memory, Fuzzy Associative Memory, and Counter Propagation. Some supervised learning NNs are Boltzmann Machine, Perceptron, Back-Propagation, and Learning Vector Quantization. The work in this thesis is built on back-propagation supervised learning algorithm [10] [19] [20].

A back-propagation NN in its basic form is composed of several layers of neurons; an input layer, one or more hidden layers, and an output layer. Each layer of neurons receives its input from the previous layer or from the network input. The output of each neuron feeds the next layer or the output the network. This is illustrated in Figure 2-6, which shows 3 layers NN. The first layer is an input layer that distributes the inputs to the hidden layer and does not have any activation function.

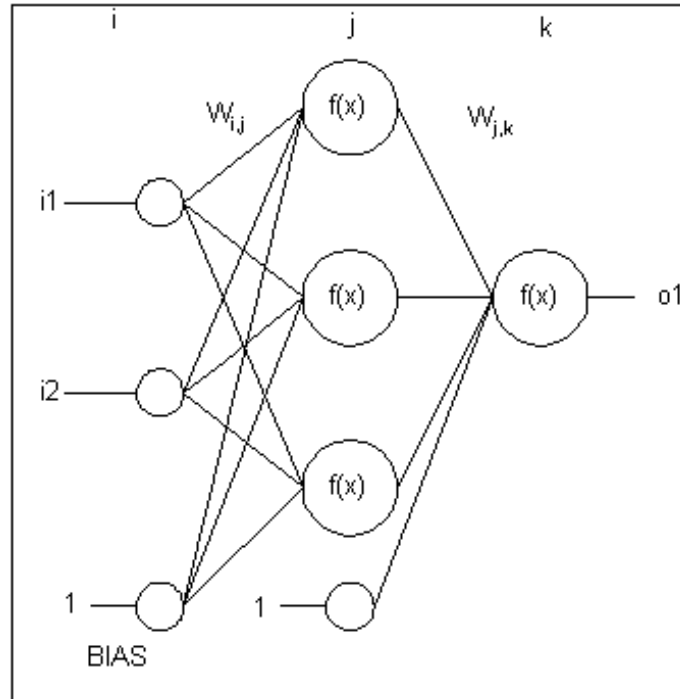


Figure 2-6: A simple 2x3x1 NN.

The lines connecting the neurons represent the weights. Also shown are the bias nodes used to shift the neuron transfer function and improves the network performance.

Mathematically the network computes:

1. The output of the hidden layer (treating the bias as another input):

$$h(j) = \sum(w(i, j) * i(i), i = 1, 3)$$

$$s(j) = f(h(j))$$

2. For the output layer calculate:

$$h'(k) = \sum(w'(j, k) * s(j), j = 1, 3)$$

$$O(k) = f(h'(k))$$

Where:

$i(i)$ - are the network inputs,

$O(k)$ - are the network outputs,

$W(i, j)$ - represents the weight connecting neuron i in layer 1 to neuron j in layer 2,

$W'(j, k)$ - represents the weight connecting neuron j in layer 2 to neuron k in layer 3,

$f(x)$ - is the neuron transfer function. For example a sigmoid: $f(x) = 1/(1 + \exp(-x))$.

Training such a network involves using a database of examples which are values for the input and output of the NN. The NN would learn by adjusting the weights to minimize the error of the outputs. The error function is the objective of the minimization procedure and defined as:

$$e = \sum_{k=1}^{Kmax} \sum_{p=1}^{Pmax} \sqrt{t(p,k) - O(p,k)} \quad (2.6)$$

Where:

$O(p,k)$ - is the NN output k for pattern p .

$t(p,k)$ - is the output training pattern p for output k .

The reported *RMS* Error is calculated as: $RMS = \sqrt{e / Pmax}$

2.5. Moment Theory

In general, moments describe numeric quantities at some distance from a reference point or axis. Moments are commonly used in statistics to characterize the distribution of random variables, and, similarly, in mechanics to characterize bodies by their spatial distribution of mass. The use of moments for image analysis is straightforward if we consider a binary or gray image segment as a two-dimensional density distribution function. In this way, moments may be used to characterize image segment and extract properties that have analogies in statistics and mechanics [21]. The two-dimensional Cartesian moment, order $(p+q)$, of a density distribution function, $f(x, y)$, is defined as

$$m_{pq} = \int_{-\infty}^{\infty} \int_{-\infty}^{\infty} x^p y^q f(x, y) \, dx \, dy \quad (2.7)$$

The two-dimensional moment for a $(N \times M)$ discretized image, $g(x, y)$, is

$$m_{pq} = \sum_{y=0}^{M-1} \sum_{x=0}^{N-1} x^p y^q g(x, y) \quad (2.8)$$

A complete moment set of order n consists of all moments m_{pq} such as $p + q \leq n$ and consists of $(\frac{1}{2})(n+1)(n+2)$ elements [21]. The use of moments for image analysis and object representation was inspired by [22]. Hu's uniqueness theorem states that if $f(x, y)$ is piecewise continuous and has no zero values only in the finite region of the (x, y) plane, then the moments of all orders exist. It can then be shown that the moment set $\{ m_{pq} \}$ is uniquely determined by $f(x, y)$ and conversely, $f(x, y)$ is uniquely determined by $\{ m_{pq} \}$.

Since an image segment has finite area and, in the worst case, is piecewise continuous, moments of all orders exist and a moment set can be computed that will uniquely describe the information contained in the image segment. To characterize all of the information contained in the image segment, potentially infinite number of moment values is required. The goal is to select a meaningful subset of moment values that contain sufficient information to uniquely characterize the image for a specific application.

The low-order moment values represent well-known, fundamental geometric properties of a distribution or body. To illustrate these properties and show the applicability to object representation, we can consider the moment values of a distribution function that is binary and contiguous, i.e. a silhouette image of a segmented object. The moment values for this distribution may be easily explained in terms of simple shape characteristics of the object.

The definition of the zeroth order moment, $\{m_{00}\}$, of the distribution, $f(x, y)$

$$m_{pq} = \int_{-\infty}^{\infty} \int_{-\infty}^{\infty} f(x, y) \, dx \, dy \quad (2.9)$$

represents the total mass of the given distribution function or image. When computed for a silhouette images for a segmented object, the zeroth moment represents the total object area.

The two first order moments, $\{m_{10}, m_{01}\}$, are used to locate the Center Of Mass (COM) of the object. The coordinates of the COM, (\bar{x}, \bar{y}) , is the intersection of the lines, $x = \bar{x}$ and $y = \bar{y}$, parallel to the x and y axis respectively, about which the first order moment is zero. Alternatively, $x = \bar{x}$ and $y = \bar{y}$ represent lines where all the mass may concentrated without change to the first order moments about the x and y axes, respectively. In terms of moment values, the coordinates of the COM are

$$\bar{x} = \frac{m_{10}}{m_{00}} \quad \text{and} \quad \bar{y} = \frac{m_{01}}{m_{00}}.$$

The COM defines a unique location with respect to the object that may be used as a reference point to describe the position of the object within the field of the view. If an object is positioned such that its COM is coincident with the origin of the field of view, i.e. $(\bar{x}=0)$ and $(\bar{y}=0)$, then the moments computed for that object are referred to as the central moments and are designated by μ_{pq} [21].

Several techniques have been demonstrated that derives invariant features from moments for object representation. Their moment definition, the type of image data exploited, and the methods for deriving invariant values from the image moments distinguish these techniques. Various moment definitions are characterized by the choice of basic functions, which may be orthogonal or non-orthogonal polynomials, and the sampling of the image, which may be rectangular or polar. Most invariant characterization achieves object scale and translation invariance through feature normalization since this is easily accomplished based on the low-order moments. The difficulty in achieving object rotation invariance has inspired much of the moment research.

Five principle moment-based invariant feature techniques may be identified from the research to date. The earliest method, Moment Invariants, is based on non-linear combination of low-order two-dimensional Cartesian moments that remain invariant under rotation. Alternative moment definitions based on polar image representations, Rotational moments, were also proposed as a solution for their simple rotation properties. Moment definitions, utilizing uncorrected basis functions and orthogonal moments, were developed to reduce the information redundancy that existed with conventional moments. Furthermore, orthogonal moments have more simply defined inverse transform, and may be used to determine the minimum number of moments requires adequately reconstructing, and thus uniquely characterizing, a given image. Related to orthogonal moments, Complex Moments provide straightforward computation on invariant moments of an arbitrary order. Finally, Standard Moments are unique in a way they achieve invariance completely through image feature normalization in moment domain rather than relying on algebraic invariance.

CHAPTER 3

FRACTAL FEATURE EXTRACTION

3.1. Introduction

The extracted feature vector should satisfy certain conditions to be a reliable feature vector. The fractal features are fractal signature (D), and NTFS. The concept of fractal dimension and its two versions are explained in details in Section 3.2. These dimensions are self-similarity dimension (Section 3.2.1) and compass dimension (Section 3.2.2). Algorithms for computing fractal dimension are explained in Section 3.3. The invariance behavior of fractal dimension under scale, rotation, and translation is provided in Section 3.3.1. While fractal dimension is considered a good feature used in classification, it suffers from some drawbacks. Fractal dimension, alone, cannot discriminate between targets of close roughness measures. Fractal signature has a better capability than fractal dimension in classification tests. However, it suffers from sensitivity to noise and high dimensionality (feature vector has 180 elements). In this chapter, a NTFS is presented. The NTFS feature vector is composed of only five elements.

As mentioned, earlier, in chapter 1, after segmentation stage, a set of features is computed for each object. The reliability of these features is essential for target classification. Most of the features used by researchers are geometric, topological, and spectral. Hu's moments are most extensively used for classification of aircraft, ships, ground targets, bridges, buildings, etc. In addition to the specific restrictions imposed by the classification techniques, the desirable properties of the features are invariance to the geometry (rotation, scale, and translation), computational efficiency, and extract ability under adverse conditions. The primary goal of feature selection stage is to obtain features which maximize the similarity of objects in the same class while minimize the similarity of objects in different classes. Features should meet computational efficiency requirements and reduce memory requirements of the classifier. Classification has been mostly done by a K-Nearest Neighbor algorithm, using projections, linear and quadratic classifiers, structural classifiers, tree-based classifiers, clustering techniques [1], and recently by using neural net classifiers and genetics [18] [20].

The features used in this thesis are mostly based on fractal geometry such as fractal dimension and fractal signature. Moments invariant have also been used for performance evaluation purposes. A complete discussion and analysis for these features will be presented in the following subsections.

3.2. Fractal Dimension Concept

It has been found that the question of length; and likewise in other cases, of area or volume; can be ill posed. Curves, surfaces, and volumes can be so complex that these ordinary measurements become meaningless. However, there is a way to measure the degree of complexity by evaluating how fast length, or surface, or volume increases with respect to smaller and smaller scales. The fundamental idea is to assume that the two quantities length, or surface, or volume on the one hand, and scale on the other hand do not vary arbitrarily but rather are related by a law, which allows to compute one quantity from the other. The kind of law which seems to be relevant is a power law of the form ($y \propto x^D$) that turns out to be very useful for the discussion of dimension. Dimension is not easy to understand. At the turn of the century it was one of the major problems in mathematics to determine what dimension means and which properties it possesses. Mathematicians have come up with some 10 different notions of dimension: topological dimension, Hausdroff dimension, fractal dimension, self-similarity dimension, box-counting dimension, capacity dimension, information dimension, Euclidean dimension, and more [16]. They are all related. Some of them, however, make sense in certain situations, but not at all in others, where alternative definitions are more helpful. Sometimes they all make sense and are the same. Sometimes several make sense but do not agree. The details can be confusing, even for a mathematician. Thus we will restrict ourselves to an elementary discussion of three of these dimensions which are special forms of Mandelbrot's fractal dimension. These dimensions are, self-similarity dimension, compass dimension, and box-counting dimension [14].

3.2.1. Self-similarity dimension

A structure is said to be (strictly) self-similar if it can be broken down into arbitrarily small pieces, each of which is a small replica of the entire structure. Here it is important that small pieces can in fact be obtained from entire structure by a similarity

transformation. The best way to think of such a transformation is what we obtain from photocopier with a reduction feature. For example, if we take a Koch curve and put it on a copying machine, set the reduction to 1/3 and produce four copies, then the four copies can be pasted together to give back the Koch curve. It then follows that if we copy each of the four reduced copies by a reduction factor of 1/3 four times, i.e. produce 16 copies which are reduced by a factor of 1/9 compared to the original. With an ideal copier, this process could be repeated infinitely often. Figure 3-1 displays a photocopier with reduction factor of 1/3.

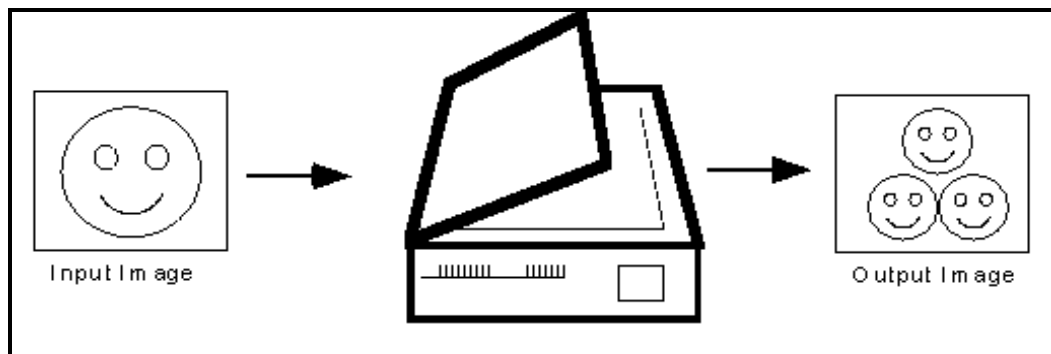


Figure 3-1: A special photcopy machine with reduction factor of 1/3.

If a structure is self-similar, it would not necessary be fractal. Example include a line segment, a square, or a cube. Each can be broken into small copies, which are obtained by similarity transformations as in Figure 3-2. These structure, however, are not fractals.

Here we see that the reduction factor is 1/3, which is, of course, arbitrary. We could as well have chosen 1/2, 1/7, or 1/354. In the latter the reduction factors (if any exist) are characteristic. For example, the Koch curve only admits 1/3, 1/9, 1/27, etc. The point, however, is common to all strictly self-similar structures (fractal or not). There is a relation between the reduction factor and the number of scaled down pieces into which the structure is divided. Apparently, for the line, square, and cube there is a nice power law relation between the numbers of pieces “*a*” and the reduction factor “*s*”. This is the law

$$a = \frac{1}{s^D}, \tag{3.1}$$

Where $D=1$ for the line, $D=2$ for the square, and $D=3$ for the cube. In other words, the exponent in the power law agrees exactly with those numbers, which are known as

topological dimensions of the line, square, and cube. If we look at the Koch curve, however, the relation of $a=4$ to $s=1/3$ and $a=16$ to $s=1/9$ is not so obvious.

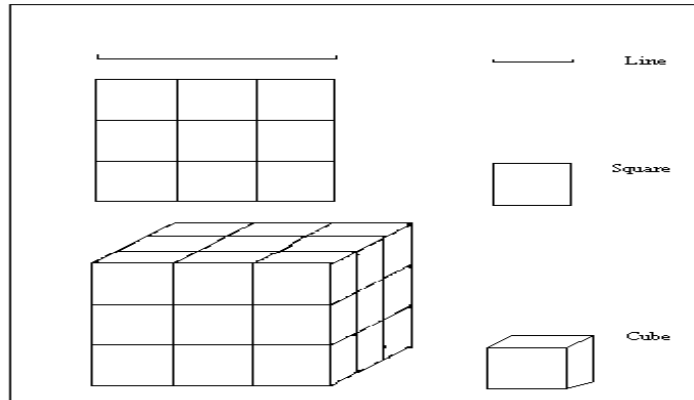


Figure 3-2: Self-similarity of line, square, and cube.

We postulate that equation (3.1) holds any way. In other words, $4 = 3^D$. Taking logarithm on both sides, we get

$$\log 4 = D \log 3,$$

or equivalently

$$D = \frac{\log 4}{\log 3} \approx 1.2619.$$

If we take smaller pieces, as with a reduction factor of $1/9$, we would postulate that $16 = 9^D$, or

$$\log 16 = D \log 9,$$

$$\text{Or } D = \frac{\log 16}{\log 9} = \frac{\log 4^2}{\log 3^2} = \frac{2 \log 4}{2 \log 3} = \frac{\log 4}{\log 3} \approx 1.2619.$$

And as a general rule, $D = \frac{\log 4^K}{\log 3^K}$ for the Koch curve.

Hence the power law relation between the number of pieces and the reduction factor gives the same number D , regardless of the scale we use for the evaluation. D is a number between 1 and 2, that we call the self-similarity dimension of the Koch curve. More generally, given a self-similar structure, there is a relation between the reduction factor s and the number of pieces a into which the structure can be divided; and that is

$$a = \frac{1}{s^D}$$

or equivalently

$$D = \frac{\log a}{\log \frac{1}{s}} \quad (3.2)$$

D is called the self-similarity dimension [16].

3.2.2. Compass dimension

Mandelbrot in 1961 came across measurements for determining the length of Britain's west coast and the Spanish-Portuguese land frontier. Based on that results Richardson had noticed that the results depended heavily on the scale of the map used. A map with 1 cm corresponding to 100 km (scale 1:10 000 000) simply shows less detail than a hiking map, in which 1 cm corresponds to 1 km (scale 1: 100 000). As we see more detail, the coastline gets longer. The same phenomenon can also be expressed by considering one map only, on which all detail can be seen, but measuring a smaller measuring unit each time. We could make a first rough estimate with a measuring unit of 100 km, and then scale this down by a factor of 10 each time. Of course the choice of a factor is rather arbitrary. The measuring unit could be reduced just as well by a factor of 2 or 3 each time. Figure 3-3 shows what Richardson actually found. In the figure, the measuring unit is plotted horizontally on a logarithm scale. We will indicate it by a . As we move to the left, a value decreases. The measured length s has been plotted vertically, also in a logarithm scale. The resulting lengths are indicated by small circles. The fact that the result turns out to be roughly on a straight line is very remarkable. For the west coast of Britain this can be expressed by the formula

$$\log s = -0.22 \log a + \log s_1$$

s_1 being the length when using a measuring unit of 1 km . The number 0.22 measures the slop of the line of results.

The formula defines a linear relationship between the logarithm of the measuring unit and the resulting length of the coastline. Without logarithms, this can be expressed as

$$s = s_1 \left(\frac{1}{a} \right)^{0.22}$$

This shows what happens when we reduce a . If a is reduced by a factor of 32, s will double. In our mind we can continue reducing further and further. Eventually this would lead us to conclude that the west coast of Britain is infinitely long [8].

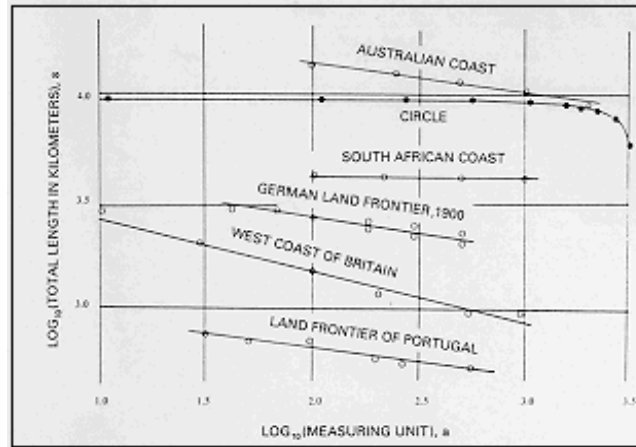


Figure 3-3: Results of Richardson's experiment

The third and final version of Mandelbrot's fractal dimension is the box-counting dimension. This concept is related to the self-similarity dimension. It gives the same numbers in many cases, but also different numbers in some others. So far, we have seen that we can characterize structures, which have some very special properties such as self-similarity, or structures like coastlines, where we can work with compass of various settings. But a problem is when a structure is not at all self-similar and as irregular as in Figure 3-4. In such case, there is no curve which can be measured with compasses; and there is no self-similarity, though there are some scaling properties. The box-counting dimension proposes a systematic measurement, which applies to any structure in the plane and can be readily adapted for structures in space. The idea is very much related to the coastline measurements. We put the structure onto a regular mesh with mesh size s , and simply count the number of grid boxes which contain some of the structure. This gives a number denoted by N . Of course, the number will depend on our choice of s . Therefore, we write $N(s)$. Now change s to progressively smaller sizes and count the corresponding number $N(s)$. Next we make a $\frac{\log(N(s))}{\log(\frac{1}{s})}$ diagram as in figure 3-3. We then try to fit a straight line to the plotted points of the diagram and measure its slope D . This number is the box-counting dimension [14].

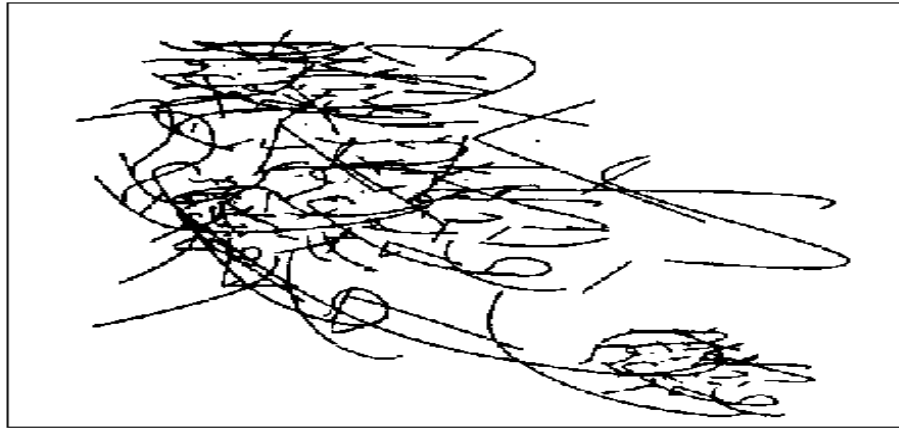


Figure 3-4: An irregular structure with some scaling properties.

3.3. Fractal dimension computation

As discussed in chapter 2, a fractal Brownian function $V_H(t)$ is a single valued function of one variable, where t is usually a time. A parameter H is in the range $0 < H < 1$, and if H is close to 0, the traces are roughest, while those with H close to 1 are relatively smooth. H relates the typical change in V ,

$$\Delta V = V(t_2) - V(t_1),$$

to the time difference $\Delta t = t_2 - t_1$ by the simple scaling law

$$\Delta V \propto \Delta t^H \tag{3.3}$$

Whereas the self-similar shapes repeat (statistically or exactly) under a magnification, the fBm traces repeat statistically only when the t and V directions are magnified by different amounts. If t is magnified by a factor r (t becomes rt), then V must be magnified by a factor r^H (V becomes $r^H V$). The variance of variations is proportional to the increment value as:

$$\sigma^2(\Delta V) \propto (\Delta t)^{2H}.$$

The variations of a fBm $V_H(t_i) - V_H(t_{i-1})$ has a Gaussian distribution each with variance:

$$\sigma^2(V_H(t_i) - V_H(t_{i-1})) \propto (t_i - t_{i-1})^{2H}.$$

then the standard deviation of the variations is

$$\sigma (V_H(t_i) - V_H(t_{i-1})) \propto (t_i - t_{i-1})^H \quad (3.4)$$

This relation is known as T^H law where

$$T^H = (t_i - t_{i-1})^H$$

The fractal dimension D , is a real value greater than the topological dimension E . The relationship between D , E and the roughness measure H is given by: $D = E+1-H$. For 1-D, $E=1$ and $D=2-H$. For 2-D, $E=2$ and $D=3-H$, [8]. The fractal dimension is scale-, rotation-, and translation-invariant.

The fitted line between the logarithm of the standard deviation, of the differences in gray levels, between pixels separated by specified vectors, and the logarithm of the vector lengths, gives H .

According to equation (3.4), we compute the standard deviation of the fractal curve variations using specified point spacing. The logarithm of the standard deviation is given by equation 3.5.

$$\log(\sigma_i) = \log(C_H) + H \log(T_i) \quad (3.5)$$

By fitting the relation between the logarithm of the point spacing and the logarithm of its corresponding standard deviation, we get D [9] [10].

The signal in Figure 3-6 shows a random variable representing the radii profile of the aircraft viewed in Figure 3-5, and the graph in Figure 3-7 shows the $\log T$ vs $\log \sigma$ relation which depends on (3.5). The slope of the line represent the roughness measure (H), the fractal dimension $D=2-H$. In our case (Figure 3-5), $H=0.9$ and $D=1.1$



Figure 3-5: The front view of Mirage 2000.

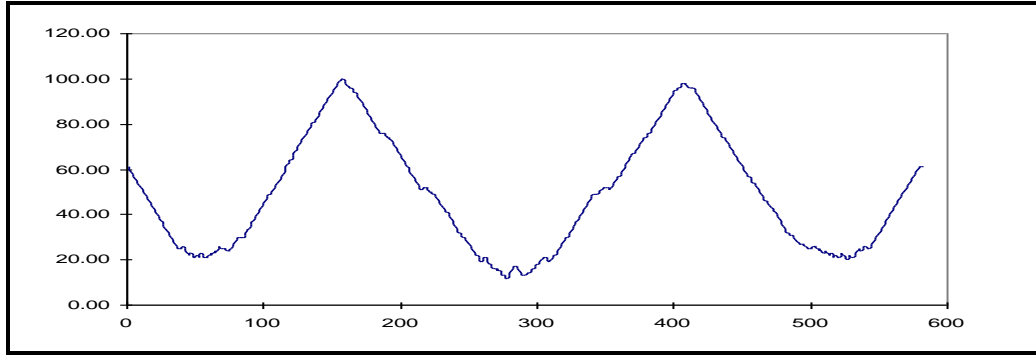


Figure 3-6: The Radii profile of the front view of Mirage 2000.

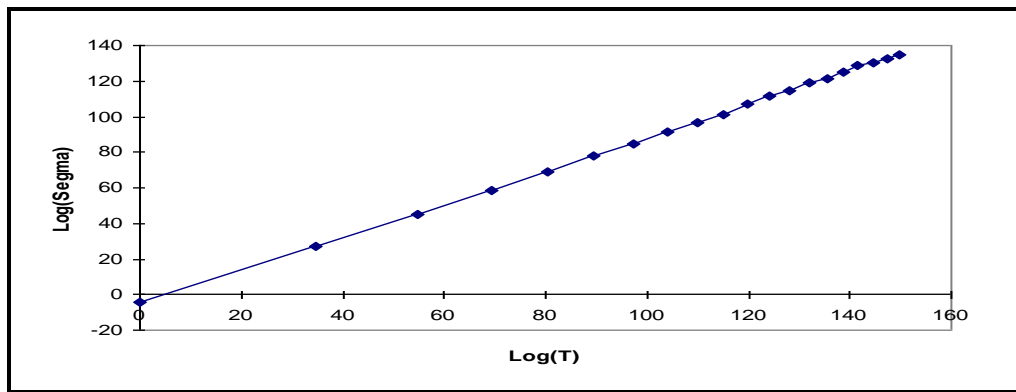


Figure 3-7: Law verification and calculation of fractal dimension (D).

Fractal dimension D is scale, translation, and rotation invariant.

3.3.1 Invariance of fractal dimension

3.3.1.1 Scale invariant

To prove that fractal dimension is scale invariant, for a fractional Brownian motion function $V_H(t)$. Let $\bar{V}_H(t)$ be the scaled version of $V_H(t)$ by scale factor λ . From an elementary geometry construction

$$\bar{V}_H(t+T) - \bar{V}_H(t) = \lambda \left[V_H(t/\lambda + T/\lambda) - V_H(t/\lambda) \right] \quad (3.6)$$

Then, from equation (3-4) and equation (3-5)

$$\sigma \left[\bar{V}_H(t+T) - \bar{V}_H(t) \right] = \lambda C_H (T/\lambda)^H = \lambda^{H-1} C_H T^H \quad (3.7)$$

By fitting the relation between the standard deviation of the variations of the scaled fBm, against the points spacing, the slope of the fitted line is H , remains the same for the

original version. This means that, the fractal dimension D is unchanged, i.e., scale invariant.

3.3.1.2 Translation invariant

The roughness measure H is estimated by the slope of the best fitted line of the relation between the logarithm of the point spacing values and the logarithm of the standard deviation of the variation of the signal corresponding to the point spacing value. When the signal is shifted or translated, the variations are still the same, and then the standard deviation values remains unchanged, so the estimated value of H remains constant for the original and the shifted signals. This means that D is translation invariant.

3.3.1.3 Rotation invariant

The signal that is rotated by a specified angle is the same as multiplying the variations values between signal amplitudes by a constant value. From the standard deviation properties, the value of the standard deviation of the rotated signal is the value of the original signal multiplied by a constant value. So the slope of the best fitted line between the logarithm of the point spacing values and the logarithm of the standard deviation of the variations remains unchanged. This means that the fractal dimension D is also rotation invariant.

Figure 3-8 and Figure 3-9 show a computed fractal dimension using the variance scaling method for different scaling and rotation angles for the front view of Mirage 2000 shown before.

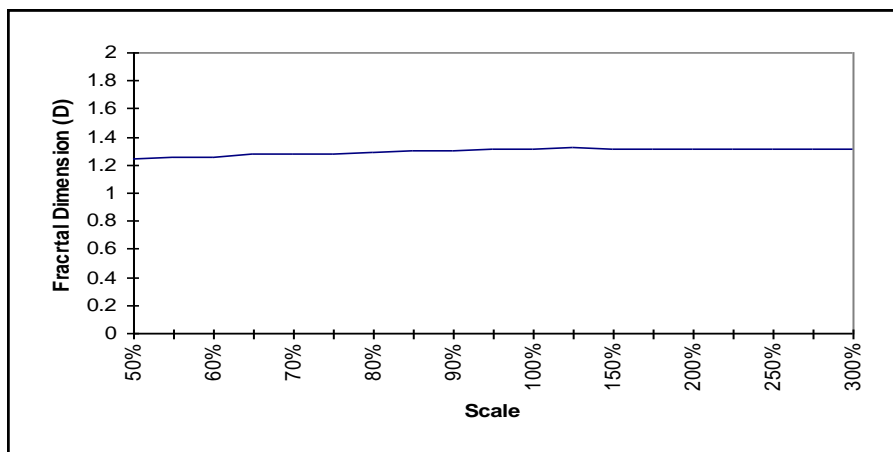


Figure 3-8: Fractal dimension at different scale percentage.

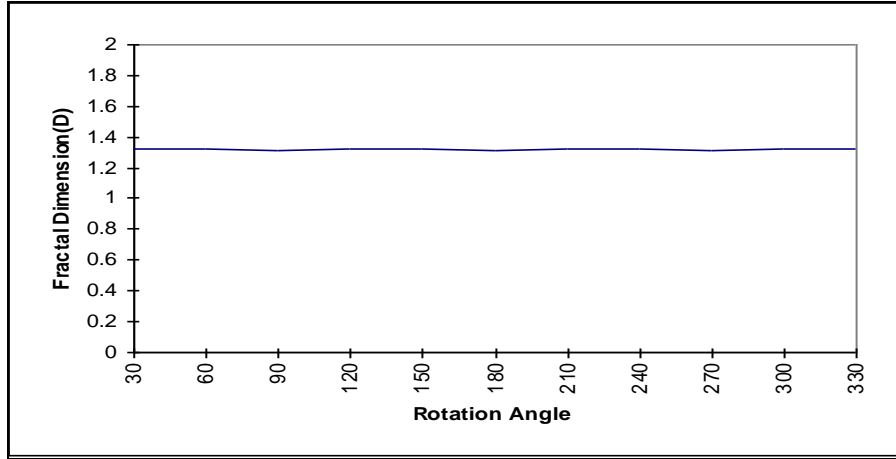


Figure 3-9: Fractal dimension at different rotational angles.

It's clear that the fractal dimension is invariant under rotation, translation, and scaling.

3.4. Fractal Signature

Fractal dimension is a good feature for discriminating classes that have different roughness but in the cases of the nearly same roughness measure, fractal dimension is not enough. Another fractal feature called fractal signature, which has a better capability for classifying signals with the same fractal dimension, has been used. 2-D shape boundary may be modeled as an *fBm*. If we consider the Boundary *B* (see Figure 3-10), then a function:

$$\varepsilon(B, \Delta\theta) = E[|r(G + \Delta\theta) - r(\theta)|]$$

where $E[|r(\theta + \Delta\theta) - r(\theta)|]$ is the expected value of the difference in radius (from centroid *c*) for any two points separated by an angle $\Delta\theta$, where *E* denotes the expectation operator [23].

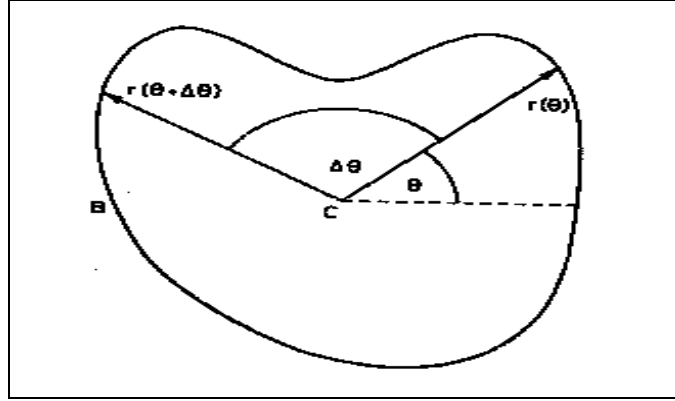


Figure 3-10: Radii profile for a boundary of a shape.

When a region is extracted from an image, we get a boundary that is made up of a list of discrete points. Then we can scan the list and generate a list of polar coordinates

$$(r_i, n_i * \theta_{\min}), i = 1, 2, \dots, N$$

where n_i is an integer, and θ_{\min} is constant. Then $N = 2\pi / \theta_{\min}$.

We can then calculate $\mathcal{E}(B, \Delta\theta)$ for integral multiples k of θ_{\min} by scanning the polar list.

$$\mathcal{E}(B, k * \theta_{\min}) = \sum_{i,j} |r_i - r_j|$$

Where $n_i - n_j = k$.

Clearly $\mathcal{E}(B, \Delta\theta)$ will have a period 2π and $\mathcal{E}(B, \Delta\theta) = \mathcal{E}(B, \pi - \Delta\theta)$, so we need only to look at values of $\Delta\theta$ between 0 and π to get a complete signature [23].

Figure 3-11 shows the signature of 3 different shapes. These three curves are clearly distinct.

Since $\mathcal{E}(B, \Delta\theta)$ is measured relative to the centroid of the shape, the fractal signature is invariant under translation. The measure used involves the difference of radii, so the signature is both rotation and reflection invariant.

Scaling of the shape would result in a similar scaling of the \mathcal{E} values and thus a constant offset in the graph. In order to overcome this, the signature can be normalized by dividing by the mean radius i.e.

$$\mathcal{E}(\theta, \Delta\theta) = E[|r(\theta + \Delta\theta) - r(\theta)|] / E(r(\theta))$$

Then the fractal signature is translation, rotation and scale invariant.

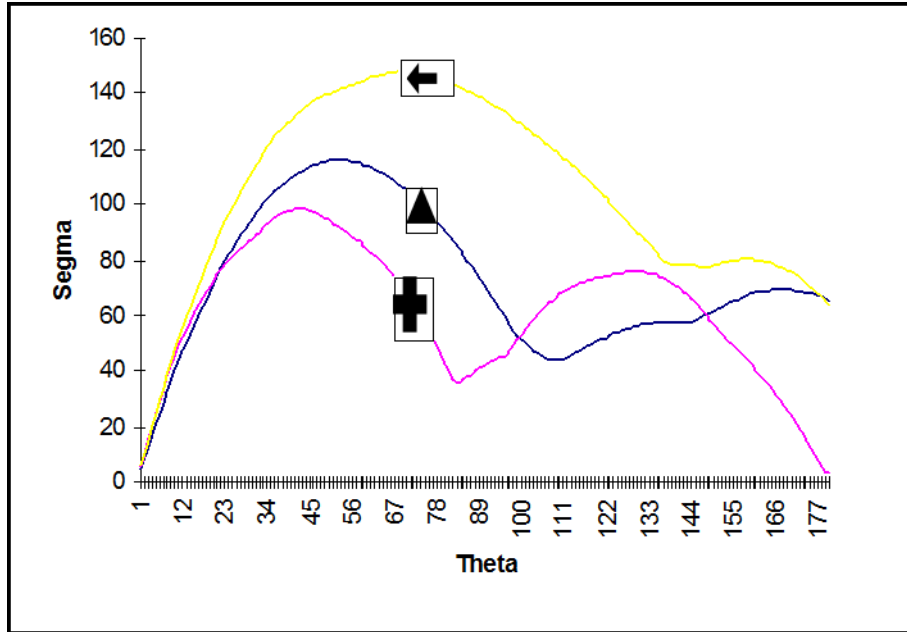


Figure 3-11: Fractal signatures for simple shapes.

CHAPTER 4

FRACTAL-BASED APPROACH FOR TARGET RECOGNITION

This chapter addresses the problem of three-view target classification. A procedure for using noise-tolerant fractal feature vector to identify a 3-D object from a 2-D image recorded at an arbitrary viewing angles and scale is presented in Section 4.3. Our approach is based on extraction of global image information from one view using regular moments in Section 4.4.

A procedure for using noise-tolerant fractal feature vector to identify a 3-D object from a 2-D image recorded at an arbitrary viewing angles and scale is presented. Three-view targets at arbitrary viewing angles and range are presented to a three-layer back propagation neural net classifier in Section 4.5. The proposed procedure is used to classify five different aircraft types. The five class types under study are Mirage 2000, B 57, Beech craft, F 15, and Tu-160. Each class type is represented by three views (front, side, top). This results in fifteen subclasses. A comparative study between the proposed fractal based classification scheme and a conventional classification scheme, the moment invariants with its 7 invariant nonlinear combinations, is performed. The classification results under normal noise effect have shown superior performance of the proposed scheme.

4.1. Three-View Fractal Target Recognition

A set of five class type of aircraft (Mirage 2000, B 57, Beech craft, F15, and Tu-160) is used in this study. Each class type is represented by three views (front, side, top). The results in fifteen subclasses are shown in Figure 4-1. The boundary of each aircraft has been shown to have fractional Brownian motion behavior. The verification of this property for Mirage 2000 side view (for example) is shown in Figure 4-2, and Figure 4-3. Three-view targets at arbitrary viewing angles and range have been presented to a three-layer back propagation neural net classifier.

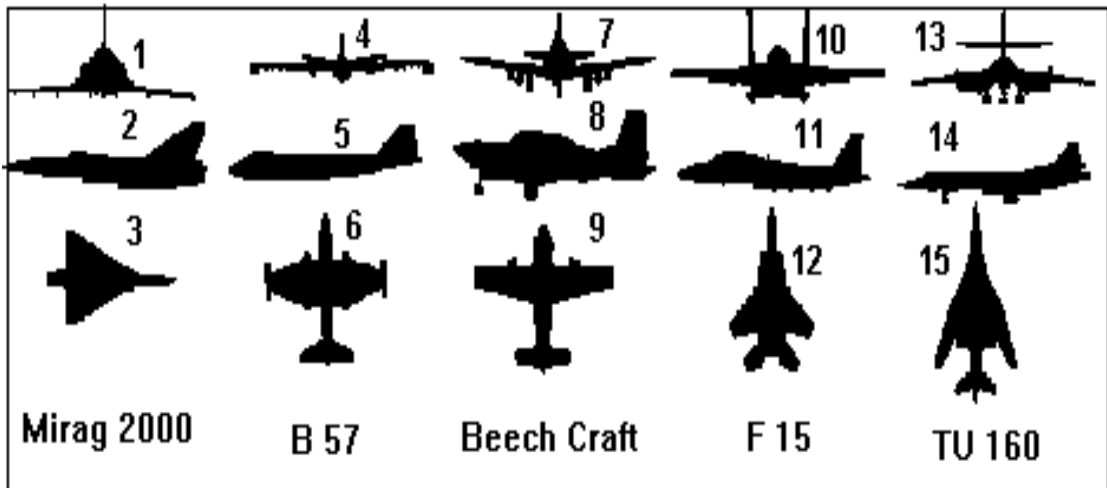


Figure 4-1: The views of the five classes of aircraft under study.

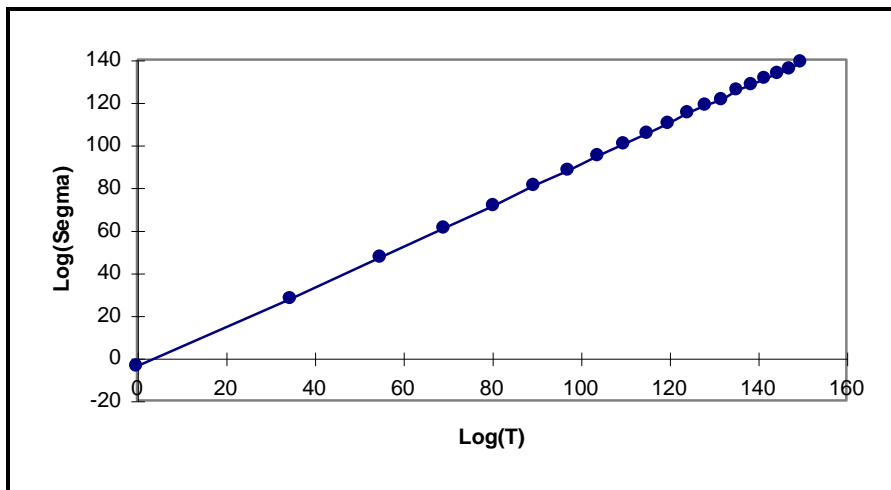


Figure 4-2: T^H verification for Mirage 2000 side view, RMSE=0.02.

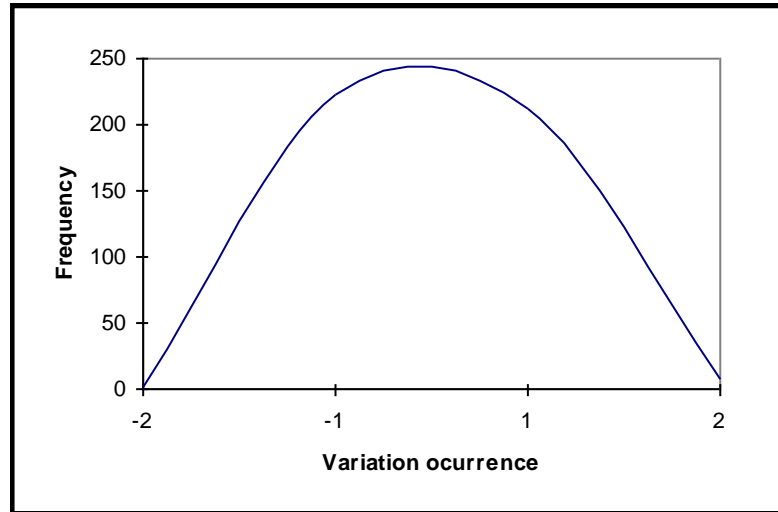


Figure 4-3: Histogram for mirage 2000 side view boundary.

4.2. Noise-tolerant fractal signature

The fractal signature feature suffers from two disadvantages. The first disadvantage is the length of the feature vector, about 180 elements. The second disadvantage is its sensitivity to noise. Figure 4-4 is adapted from [23], and shows the noise effect on the fractal signature compared to Fourier descriptors. The effect of noise on fractal signature is more than the noise effect on Fourier descriptor.

To overcome these disadvantages, a polynomial fit for the fractal signature is performed, to produce an abstracted fractal signature. Figure 4-5 and Figure 4-6 show the effect of noise on the fractal signature, and the abstracted fractal signature. If we compare Figure 4-5 and Figure 4-6 we will find that the abstracted fractal signature curves is more compact and have less deviation that the fractal signature. This can be easily interpreted as the abstracted fractal signature is more robust under noise than the fractal signature. The graph in Figure 4-6 is the fractal signature in the form

$$y = a_4x^4 + a_3x^3 + a_2x^2 + a_1x + a_0.$$

For example, the parameters of the fractal signature of some aircraft views are shown in Table 4-1

Table 4-1: Fractal abstracted signature of some aircraft views.

Aircraft view	a_4	a_3	a_2	a_1	a_0
Mirage 2000 Side View	0.000001	-0.00019	-0.02596	5.866685	8.525139
B 57 Side View	0	-0.00004	-0.04343	6.642889	0.190537
Beech Craft Side View	0.000001	-0.00022	-0.01257	4.519167	8.822295
F 15 Side View	0.000001	-0.00019	-0.02612	6.031808	6.341545
TU 160 Side View	0	0.000014	-0.04658	6.462349	2.879691

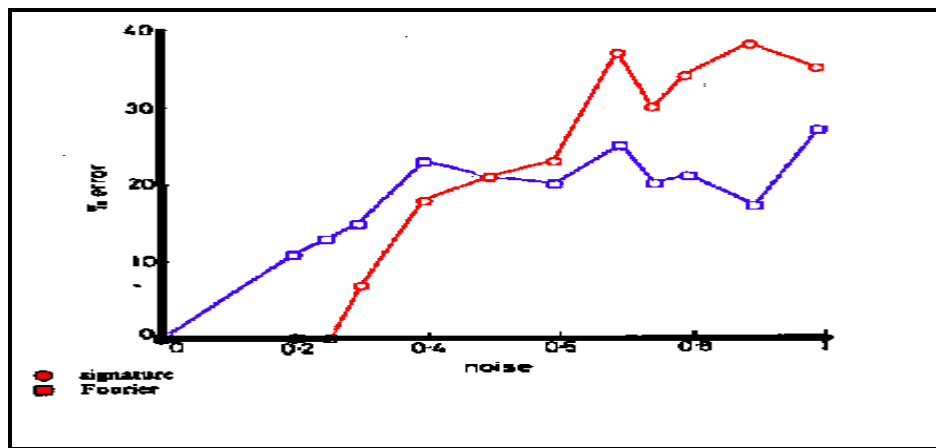


Figure 4-4: Robustness of signature and Fourier descriptors.

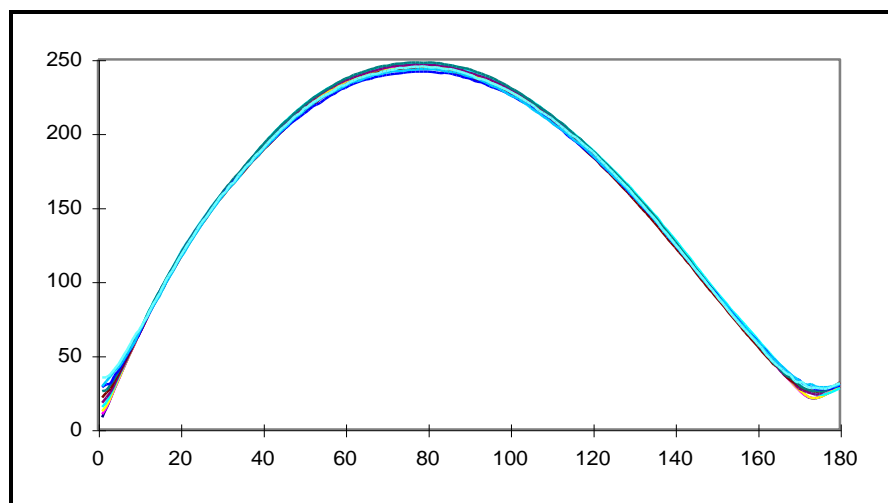


Figure 4-5: Fractal signature with different noise values.

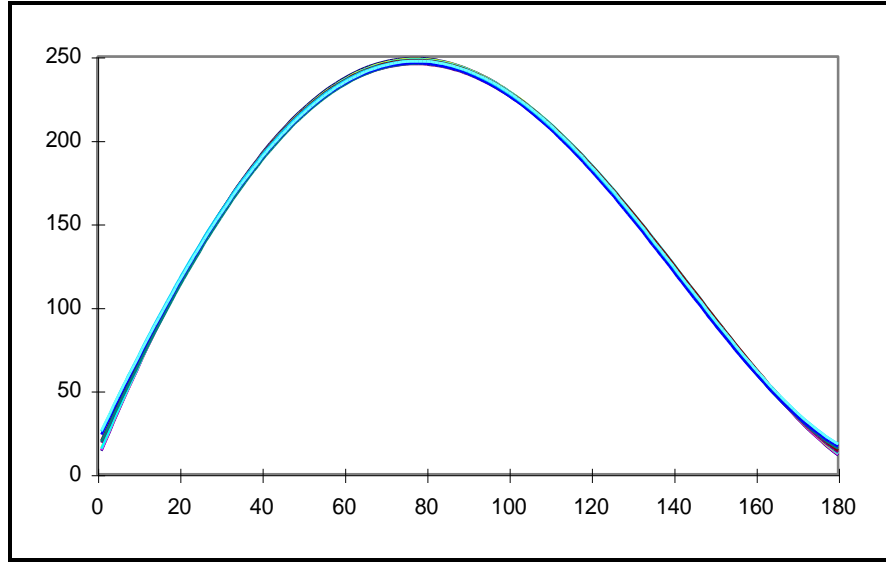


Figure 4-6: Abstracted fractal signature with different noise values.

4.3. Moments invariant

The first significant work considering moments for pattern recognition was performed by [22]. HU derived relative and absolute combinations of moments values that are invariant with respect to scale, position, and orientation; based on theories of invariant algebra. Size invariant moments are derived from algebraic invariant but can be shown to be the result of simple size normalization. Translation invariance is achieved by computing moments that have been translated by negative distance to the centroid. The set of absolute moment invariant consists of a set of non-linear combinations of central moment values that remain invariant under rotation. Hu defines seven values, computed from central moments through order three, that are invariant to object scale, position, and orientation [21].

For a digital image stored in a two-dimensional array, the moment of order $(p+q)$ is given by:

$$m_{pq} = \sum_{x=0}^{M-1} \sum_{y=0}^{N-1} x^p y^q f(x, y), \quad p, q=0,1,\dots,\infty \quad (4.11)$$

Where M and N are the horizontal and vertical dimensions of the image, respectively; and $f(x, y)$ is the intensity (gray level) at a point (x, y) in the image.

From equation (3.8), the zero-order moment

$$m_{00} = \sum_{x=0}^{M-1} \sum_{y=0}^{N-1} f(x, y)$$

is the sum of pixel values of an image. If $f(x, y)$ is a binary image, then its zero-order moment represents its area. The centroid, called the center of gravity, is computed as:

$$\bar{x} = \frac{m_{10}}{m_{00}}, \quad \bar{y} = \frac{m_{01}}{m_{00}}$$

The centroid is the balance point of the image function $f(x, y)$ such that the mass of $f(x, y)$ left and right of \bar{x} ; and above and below \bar{y} , is equal. The central moments of order $(p + q)$ are defined as follows:

$$\mu_{pq} = \sum_{x=0}^{M-1} \sum_{y=0}^{N-1} (x-\bar{x})^p (y-\bar{y})^q f(x, y) \quad (4.12)$$

Hu defines seven values, computed from central moments through order three, that are invariant to object scale, position, and orientation. In terms of the central moments, the seven moment invariant are given by

$$\begin{aligned} M_1 &= \mu_{20} + \mu_{02} \\ M_2 &= (\mu_{20} - \mu_{02})^2 + 4\mu_{11}^2 \\ M_3 &= (\mu_{30} - 3\mu_{12})^2 + (3\mu_{21} - \mu_{03})^2 \\ M_4 &= (\mu_{30} + \mu_{12})^2 + (\mu_{21} + \mu_{03})^2 \\ M_5 &= (\mu_{30} - 3\mu_{12})(\mu_{30} + \mu_{12})[(\mu_{30} + \mu_{12})^2 - 3(\mu_{21} + \mu_{03})^2] \\ &+ (3\mu_{21} - \mu_{03})(\mu_{21} + \mu_{03})[3(\mu_{30} + \mu_{12})^2 - (\mu_{21} + \mu_{03})^2] \\ M_6 &= (\mu_{20} - \mu_{02})[(\mu_{30} + \mu_{12})^2 - (\mu_{21} + \mu_{03})^2] \\ &+ 4\mu_{11}(\mu_{30} + \mu_{12})(\mu_{21} + \mu_{03}) \\ M_7 &= (3\mu_{21} - \mu_{03})(\mu_{30} + \mu_{12})[(\mu_{30} + \mu_{12})^2 - 3(\mu_{21} + \mu_{03})^2] \\ &- (\mu_{30} - 3\mu_{12})(\mu_{21} + \mu_{03})[3(\mu_{30} + \mu_{12})^2 - (\mu_{21} + \mu_{03})^2] \end{aligned}$$

Figure 4-7 and Figure 4-8 show moment invariants parameters for Mirage 2000 front view for different scaling and rotational angles, respectively.

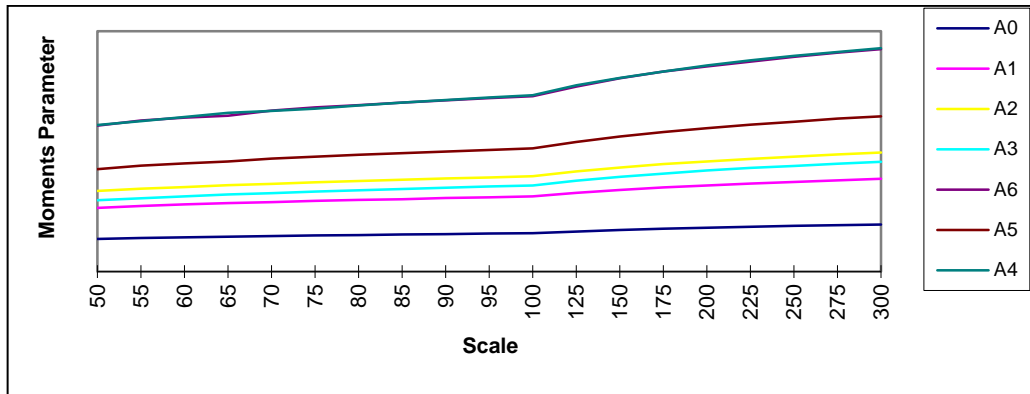


Figure 4-7: Moments invariant parameters for different scaling values.

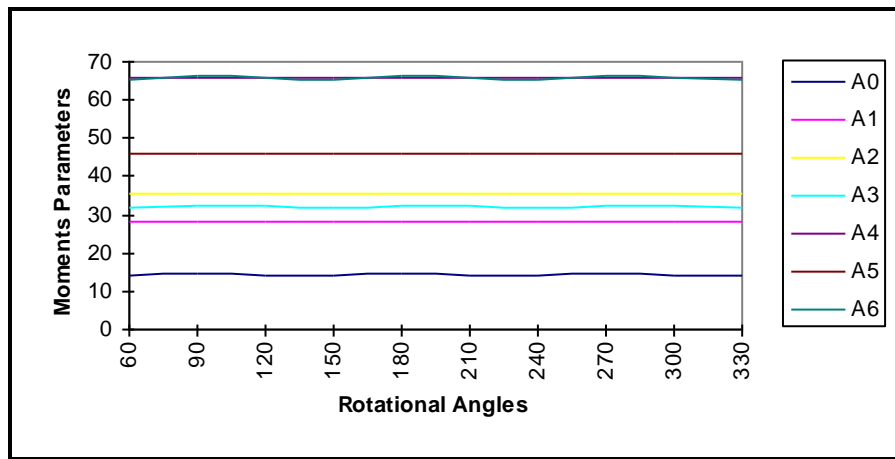


Figure 4-8: Moments invariant parameters for different rotational angles.

4.4. Classification results and discussion

Classifier performance evaluation has been performed with 40 samples for each subclass in the presence of noise. The classification results have been tabulated in a confusion matrix format. The average percentage of the correct recognition is about 98%. A comparative study between the proposed fractal based classification and a classical classification, the moments invariant with its 7 invariant nonlinear combination of central moments is performed [24] [25] [21]. The classification results using moment invariants has been performed using 30 samples from each class with total of 450 samples from the same set (shown in Table 4-2). The average percentage of correct recognition is about 95%. The performance of the two classifiers has been evaluated under noise effect.

A normal noise with zero mean and variable variance is added to the aircraft's views. Figure 4-9 depicts aircraft view with different noise levels. A representative set of clean and noisy aircraft images is shown in Figure 4-10. Classification results under noise effect are depicted in Figure 4-11. The proposed noise-tolerant fractal signature provided superior performance over moment invariants method. Under noise effect of standard deviation equal two, the percentage of correct recognition has been about 90% for the proposed system, and about 40% for the moment invariants method.

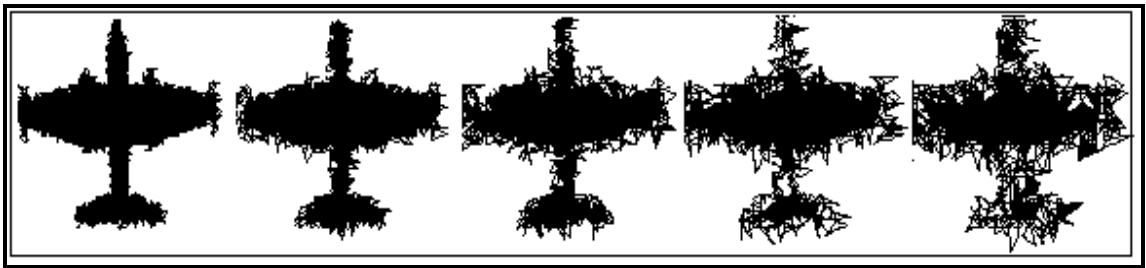


Figure 4-9: B57 front view with normal noise of zero mean and standard deviation values: 1, 2, 3, 4, 5 from left to right respectively.

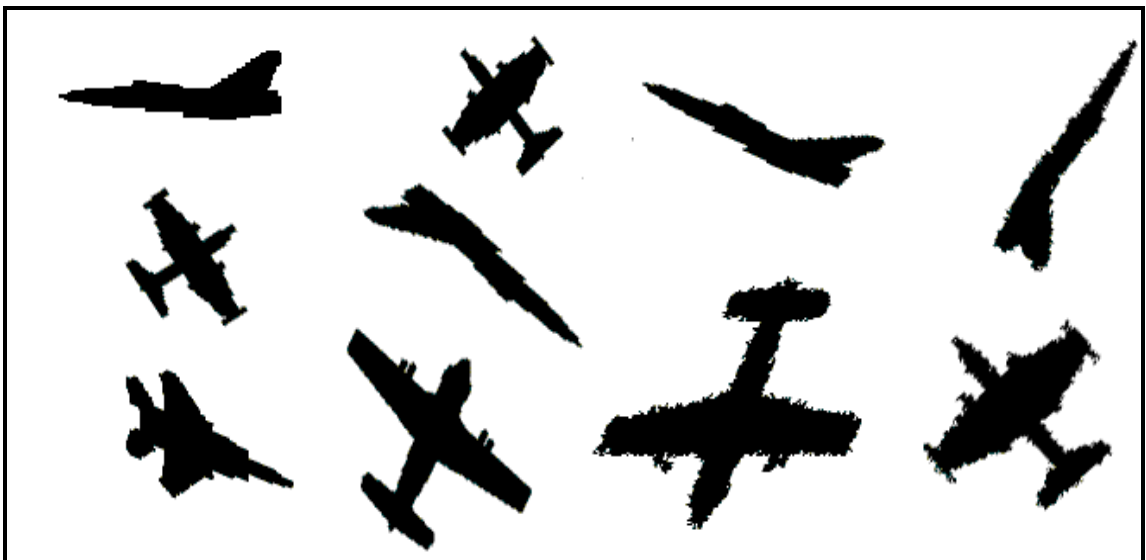


Figure 4-10: Representative example of clean and noisy test images.

Table 4-2: Confusion matrix of the results of neural net classifier with abstracted fractal signature input.

	1	2	3	4	5	6	7	8	9	10	11	12	13	14	15	Recognition Rate
1	40	0	0	0	0	0	0	0	0	0	0	0	0	0	0	1
2	0	38	0	0	0	0	0	0	0	0	0	0	0	0	0	0.95
3	0	0	40	0	0	0	0	0	0	0	0	0	0	0	0	1
4	0	0	0	40	0	0	0	0	0	0	0	0	0	0	0	1
5	0	0	0	0	40	0	0	0	0	0	0	0	0	3	0	1.075
6	0	0	0	0	0	40	0	0	0	0	0	0	0	0	0	1
7	0	0	0	0	0	0	40	0	0	0	0	0	0	0	0	1
8	0	0	0	0	0	0	0	40	0	0	0	0	0	0	0	1
9	0	0	0	0	0	0	0	0	40	0	0	0	0	0	0	1
10	0	0	0	0	0	0	0	0	0	40	0	0	0	0	0	1
11	0	2	0	0	0	0	0	0	0	0	39	0	0	2	0	1.075
12	0	0	0	0	0	0	0	0	0	0	0	40	0	0	0	1
13	0	0	0	0	0	0	0	0	0	0	0	0	40	0	0	1
14	0	0	0	0	0	0	0	0	0	0	0	0	0	35	0	0.875
15	0	0	0	0	0	0	0	0	0	0	0	0	0	0	40	1
% Correct Recog.	100	95	100	98	100	100	87.5	100								

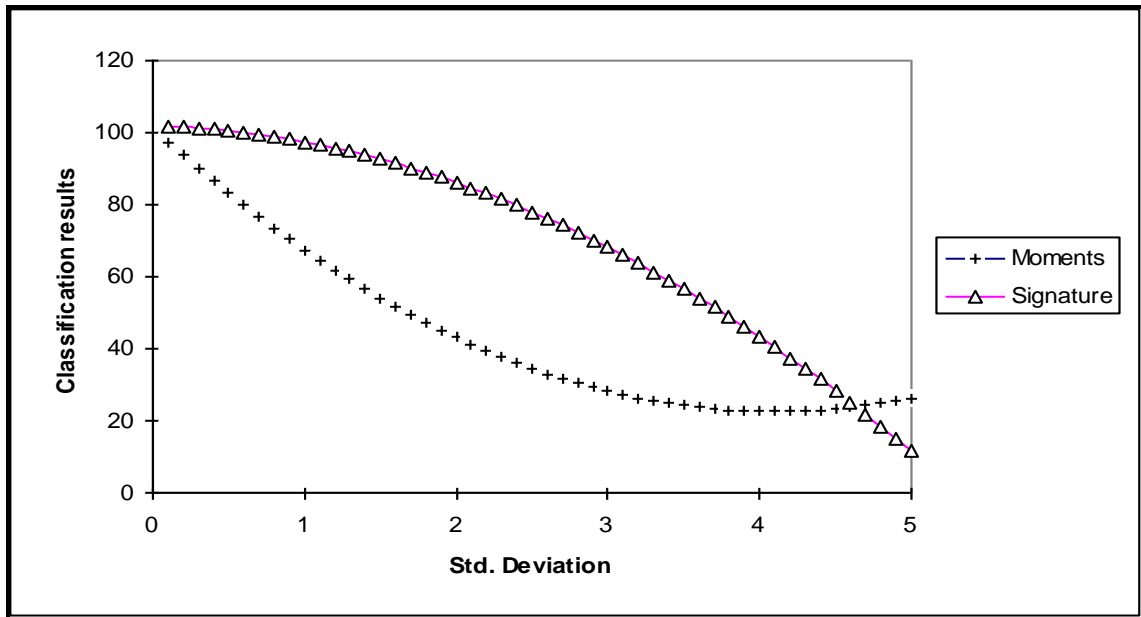


Figure 4-11: Classification results of abstracted fractal signature and moments invariant under different degrees of noise.

The system performance has been evaluated according to the set of training and learning three-view samples shown in Figure 4-1, and the system has achieved the percentage of correct recognition as shown in Table 4-2. The system has shown tolerant and reliable performance under noise effect and other arbitrary views derived and resulted from the original general views (translation, rotation, scaling).

The system can be extended to accommodate other intermediate views between the basic three-view samples to cover all target maneuver resulted in a 3-D shape specific views. The same concept and approach will be applied, except that the target will be defined by n views instead of 3 views.

The system has been tested against new views generated from 3-D rotation (pitching, rolling) as shown in Figure 4-12. Table 4-3 shows the result of recognition for different pitching, and rolling.

Table 4-3: Recognition results for tilt and yaw operations.

No	Roll	Pitch	Result Of Recognition
1	20	0	TRUE
2	40	0	FALSE
3	60	0	FALSE
4	0	20	TRUE
5	0	40	TRUE
6	0	60	TRUE
7	20	0	TRUE
8	40	0	TRUE
9	60	0	TRUE
10	0	20	TRUE
11	0	40	TRUE
12	0	60	FALSE

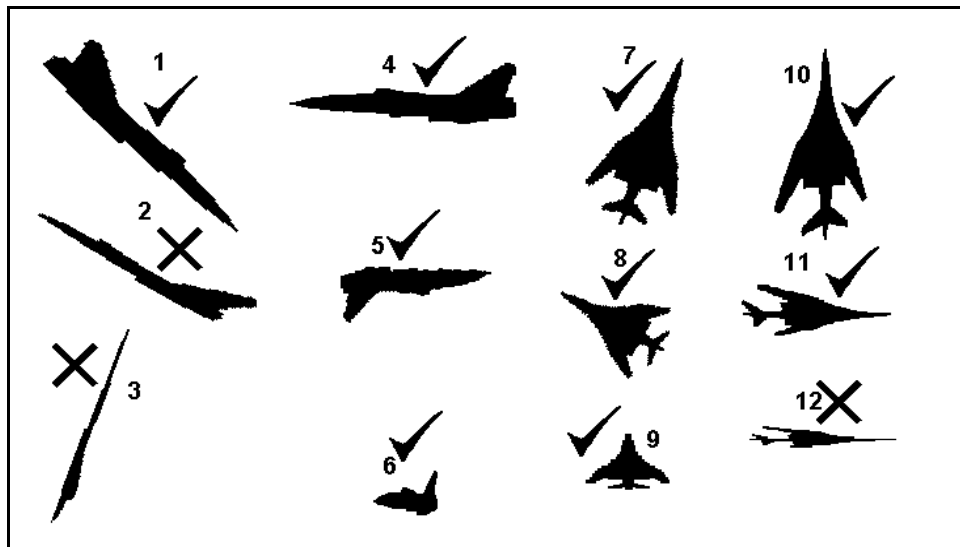


Figure 4-12: Aircraft views samples at different orientations.

CHAPTER 5

CONCLUSIONS

5.1. Conclusions

In this thesis the problem of automatic target recognition based on fractal geometry has been addressed. The following main problems have been researched:

(a) Study of the fractional Brownian motion behavior of three-view (Top, Side, Front) of five types of aircraft (Mirage-2000, B57, Beech Craft, F15, TU-160), with total of fifteen images, as well as the background objects (mountain, and tree lines),

(b) Fractal feature extraction with focus on: fractal dimension and noise-tolerant fractal signature,

(c) Application of neural net for classification of aircraft views based on the noise-tolerant fractal signature feature vector,

(d) A comparative study among the following: The abstracted noise-tolerant fractal signature, fractal signature & Fourier descriptors, and moments invariant in the classification robustness, especially under different levels of noise.

5.2. Future Research Plan

One major potential research area is the extension of the three-view target recognition to cover 3-D Aircraft images, and respond with the target class in an animated and simulated flight-maneuvering scenario.

REFERENCES

- [1] B. Bhanu, "Automatic target recognition: state of the art survey," *Aerospace and Electronic Systems, IEEE Transactions on*, no. 4, pp. 364-379, 1986.
- [2] H. Xu, G. Zhai and X. Yang, "Single Image Super-resolution With Detail Enhancement Based on Local Fractal Analysis of Gradient," *IEEE transactions on circuits and systems for video technology*, vol. 23, no. 10, pp. 1740-1754, 2013.
- [3] W. Yue, B. Yu and J. Wu, "Application of ArcGIS in fractal analysis of rivers," in *Geoinformatics, 2011 19th International Conference on*, 2011.
- [4] M. M. Chelehghi, K. Jaferzadeh and M. Nia, "A high speed intelligent classification algorithm for fractal image compression using DCT coefficients," in *Communication Software and Networks (ICCSN), 2011 IEEE 3rd International Conference on*, 2011.
- [5] K. Jaferzadeh, K. Kiani and S. Mozaffari, "Acceleration of fractal image compression using fuzzy clustering and discrete-cosine-transform-based metric," *Image Processing, IET*, vol. 6, no. 7, pp. 1024-1030, 2012.
- [6] E. A. Al-Hilo and L. E. George, "Speeding-Up Fractal Colored Image Compression Using Moments Features," in *Computing: Techniques and Applications, 2008. DICTA'08. Digital Image*, 2008.
- [7] E. A. Al-Hilo and L. E. George, "Study of Fractal Color Image Compression Using YUV Components," in *Computer Software and Applications Conference (COMPSAC), 2012 IEEE 36th Annual*, 2012.
- [8] B. B. Mandelbrot, *The fractal geometry of nature*, Macmillan, 1983.
- [9] A. P. Pentland, "Fractal-based description of natural scenes," *Pattern Analysis and Machine Intelligence, IEEE Transactions on*, no. 6, pp. 661-674, 1984.
- [10] J. M. Keller, R. M. Crownover and R. Y. Chen, "Characteristics of natural scenes related to the fractal dimension," *Pattern Analysis and Machine Intelligence, IEEE Transactions on*, no. 5, pp. 621-627, 1987.

- [11] G. G. Medioni and Y. Yasumoto, "A note on using the fractal dimension for segmentation," in *Proc. IEEE Computer Vision Workshop*, 1984.
- [12] J. M. Keller, S. Chen and R. M. Crownover, "Texture description and segmentation through fractal geometry," *Computer Vision, Graphics, and Image Processing*, vol. 45, no. 2, pp. 150-166, 1989.
- [13] N. Yokoya, K. Yamamoto and N. Funakubo, "Fractal-based analysis and interpolation of 3D natural surface shapes and their application to terrain modeling," *Computer Vision, Graphics, and Image Processing*, vol. 46, no. 3, pp. 284-302, 1989.
- [14] H.-O. Peitgen, Hartmut and D. Saupe, *Chaos and fractals: new frontiers of science*, Springer, 2004.
- [15] S. S. Chen, J. M. Keller and R. M. Crownover, "On the calculation of fractal features from images," *Pattern Analysis and Machine Intelligence, IEEE Transactions on*, vol. 15, no. 10, pp. 1087-1090, 1993.
- [16] H.-O. Peitgen, D. Saupe, M. F. Barnsley, Y. Fisher and M. McGuire, *The science of fractal images*, Springer New York etc., 1988.
- [17] M. Finlay and K. A. Blanton, *Real-world fractals*, M&T Books, 1993.
- [18] R. Lippmann, "An introduction to computing with neural nets," *ASSP Magazine, IEEE*, vol. 4, no. 2, pp. 4-22, 1987.
- [19] A. Svardström, "Neural network feature vectors for sonar targets classifications," *The Journal of the Acoustical Society of America*, vol. 93, p. 2656, 1993.
- [20] M. V. Shirvaikar and M. M. Trivedi, "A neural network filter to detect small targets in high clutter backgrounds," *Neural Networks, IEEE Transactions on*, vol. 6, no. 1, pp. 252-257, 1995.
- [21] R. J. Prokop and A. P. Reeves, "A survey of moment-based techniques for unoccluded object representation and recognition," *CVGIP: Graphical Models and Image Processing*, vol. 54, no. 5, pp. 438-460, 1992.
- [22] M.-K. Hu, "Visual pattern recognition by moment invariants," *Information Theory, IRE Transactions on*, vol. 8, no. 2, pp. 179-187, 1962.
- [23] R. Taylor and P. Lewis, "2D shape signature based on fractal measurements," *IEE Proceedings-Vision, Image and Signal Processing*, vol. 141, no. 6, pp. 422-430, 1994.

- [24] S. Maitra, "Moment invariants," *Proceedings of the IEEE*, vol. 67, no. 4, pp. 697-699, 1979.
- [25] M. R. Teague, "Image analysis via the general theory of moments*," *JOSA*, vol. 70, no. 8, pp. 920-930, 1980.
- [26] P. F. Walker, "Smart weapons in naval warfare," *Scientific American*, vol. 248, pp. 53-61, 1983.